

Ab-initio calculation of electron-boson coupling in highly-doped hafnium disulfide



Masterarbeit im Studiengang
“Master of Science” im Fach Physik an der
Mathematisch-Naturwissenschaftlichen Fakultät
der Christian-Albrechts-Universität zu Kiel

von Christoph Emeis

2022

1. Gutachter: Prof. Dr. Fabio Caruso
2. Gutachter: Prof. Dr. Kai Rossnagel

Contents

1. Introduction	1
1.1. Background and motivations	1
1.2. Overview of the thesis	2
2. Theory and Methods: First principle description of many-body systems	3
2.1. Electronic structure of solids	3
2.1.1. Density-functional theory	3
2.1.2. Numerical methods	8
2.2. Interacting systems and excited states	11
2.2.1. RPA dielectric function and plasmons	11
2.2.2. Computation of the electron-boson coupling	15
2.3. Photoemission signatures of plasmonic polarons	17
2.3.1. Angle-resolved photoemission spectroscopy (technique)	18
2.3.2. Spectral function and cumulant expansion	22
3. Electron-boson interaction in hafnium disulfide	25
3.1. Transition-metal dichalcogenides	25
3.1.1. Crystal structure Hafnium disulfide	26
3.2. Experimental conditions	27
3.3. Computational details	27
3.4. Preliminary analyses	28
3.4.1. Convergence studies	28
3.5. Electronic and vibrational properties	29
3.5.1. Spin-orbit coupling	31
3.5.2. Effective mass calculation	31
3.5.3. Iso-energy cuts and Wannier interpolation	33
3.5.4. Phonon dispersion	35
3.6. Doping and electron-plasmon interaction	36
3.6.1. Doping concentration and Fermi energy	36
3.6.2. Electron-plasmon coupling	37
3.7. Spectral features	40
4. Conclusions and Outlook	45
A. Appendix	47
Bibliography	51

List of Abbreviations

- 2D** two-dimensional
- 3D** three-dimensional
- ARPES** angle-resolved photoemission spectroscopy
- BOA** Born–Oppenheimer approximation
- BZ** Brillouin zone
- BvK** Born-von-Karman
- CBM** conduction band minimum
- DFT** density-functional theory
- DESY** German electron-synchrotron radiation source
- EPW** Electron-Phonon-Wannier
- GGA** generalized gradient approximation
- HEG** homogeneous electron gas
- HfS₂** hafnium disulfide
- HP** high symmetry point
- KS** Kohn-Sham
- LDA** local density approximation
- ONCV** optimised norm-conserving Vanderbilt
- PBE** Perdew, Burke and Ernzerhof
- PP** pseudopotential
- RPA** random phase approximation
- SOC** spin–orbit coupling
- TMD** transition-metal dichalcogenide
- VBM** valence band maximum

1. Introduction

1.1. Background and motivations

The field of many particle physics and the fundamental laws of nature hidden behind it are fascinating. In condensed matter particles come together and form a solid leading to emergent phenomena the single particles themselves did not exhibit. These include collective behaviours and elementary excitations, e.g., of the electron density, which describes the ensemble of all electrons in the system of atoms under consideration. Quantised fluctuation of the electron density are called plasmon, while collective excitations of nuclei lattice vibrations are called phonons and both can be found in a wide range of materials. They influence the physical properties of materials and accommodate a lot of potential for technological applications. [1]

A convincing way of investigating these many-particle effects is the examination of the spectral function $A(\mathbf{k}, \omega)$. The spectral function specifies the probability distribution with which particles, here electrons, are in a state with the specific energy ω and a certain momentum \mathbf{k} . It can be obtained both experimentally and theoretically by angle-resolved photoemission spectroscopy (ARPES) [2] and modern *ab-initio* calculations [3–5], respectively. ARPES enables the direct measurement of the populated states of the electronic band structure incorporating many-particle interactions. In this technique electrons are photoemitted from a sample by the interaction with light pulses and are measured angle- and energy-resolved. Since the electrons interact with the many-particle system of the solid in the photoemission process, they take the information about the system with them.

To quantify and understand the origin of the spectral function features obtained by the experiment, theoretical descriptions of the photoemission process and the interaction strength between the electrons and the different collective excitation's are required. The theoretical description and the actual computation of $A(\mathbf{k}, \omega)$ for real materials has been the topic of recent publications. [6–8] Findings include electron-plasmon and electron-phonon coupling in TiO_2 [9], EuO [10] and MoS_2 [11], which can alter carrier lifetimes, mobilities and the optical gap and could lead to custom-made optical and electronic properties desired for electronic devices like nanoelectronics [12] and photovoltaics [13, 14].

A critical parameter in the exploration and exploitation of many-particle effects is the level of the doping applied to the material. It determines which the scattering mechanism responsible for hot-carrier relaxation is dominant in the doped material and could be tuned to favor a certain type of interaction [4]. Though it brings forth a whole wealth of many-particle phenomena, the effect of doping is hardly explored for all materials interesting for technological applications. To enlighten this darkness a little bit, in this

thesis the material hafnium disulfide (HfS_2) is studied rigorously.

HfS_2 is a semiconductor that has favorable basic electronic properties for technological application in electronic devices like transistors [15]. Furthermore it exhibits many-body phenomena including the emergence of excitons [16] and plasmons [17]. Its polar composition of Hf and S make it easy to dope and thereby possible to tune its physical properties [18]. The motivation for the investigation of this specific material came with the ARPES measurements conducted by the Rossnagel group of the Kiel University. In the spectral function of the doped HfS_2 measured by them, there is clear evidence for many-particle interactions. Understanding origin of the spectral function features and identifying the dominant type of the electron-boson coupling in this material is the aim of this thesis. Thereby, the experimental data, which encodes the physical properties of the material, is supposed to be reproduced as close as possible by *ab-initio* calculations.

1.2. Overview of the thesis

The thesis is organised as follows: in chapter 2, fundamental theories describing ground state and excited state systems and their approximations enabling the computation of the electronic, vibrational and emergent properties from first-principles are presented. These include the Kohn-Sham density-functional theory (DFT) for ground state calculations and its practical implementation using plane-wave pseudopotential methods. Furthermore, the basis of the linear response theory to account for collective charge density excitations and their coupling to electrons in the framework of the random phase approximation (RPA) dielectric function is reviewed. Thereafter, the powerful and popular ARPES technique for studying real quantum materials is reviewed and a short description of the measured ARPES photocurrent using Fermi's golden rule and the momentum conservation rules is provided. Lastly, the description of the spectral function using the single-particle Green's function and the cumulant expansion is outlined.

In chapter 3, the theory is applied to the calculation of pristine and doped bulk properties of HfS_2 and the results are compared with the experimental findings in detail. First, the class of transition-metal dichalcogenides (TMDs), the crystal structure of HfS_2 and the basic procedure for every electron structure calculation are introduced. Then the band structure and the influence of the van der Waals gap, the spin-orbit coupling (SOC) and the band dispersion on the electronic and vibrational properties of HfS_2 are investigated. The study of the n-type doped HfS_2 follows thereafter. These begin with the evaluation of the measurement data to determine the free electron density caused by the doping and the calculation of the Fermi energy for this charge carrier concentration. The electron-plasmon self energy and electronic smearing parameter η are illustrated comprehensively and finally the spectral function is examined. In that process, a simplistic model for the interface dielectric function is formulated and its effect on the spectral function features is quantitatively validated. In chapter 4, the findings are summarized and an outlook is given concluding the thesis.

2. Theory and Methods: First principle description of many-body systems

In the first-principles description, the physical properties of materials are determined without the use of experimentally obtained external data. This description requires a solid theoretical basis, with approximations only being made if they are justifiable and do not misrepresent the true underlying properties of the material in question.

In this chapter, the theory and methods needed to understand and perform solid-state calculation are discussed. Firstly, the basic electronic structure theory for the calculations of the electronic properties of ground-state systems and concepts for its numerical implementation are presented. With the information about the ground-state system as a foundation, the interacting system and excited states can be described by linear response theory. It enables the characterization of the dielectric function, the formation of plasmons and the coupling between electrons and these excited states. The emergence of plasmons and other types of bosonic excitations, like phonons, can be verified by photoemission spectroscopy. Ultimately, the theoretical description of the spectral function in the Fan-Migdal approximation of the electron self-energy and its improvement in the description of satellite structures in photoemission spectra by the cumulant expansion are outlined.

2.1. Electronic structure of solids

The greatest success for first-principles description was the formulation of the DFT [19]. It is the foundation of modern *ab-initio* calculations and, since the necessary computing capacities have been available, it has become one of the most widely employed theoretical approaches for the description of quantum materials. [20]

2.1.1. Density-functional theory

The starting point of DFT is the time-independent Schrödinger equation:[21]

$$\hat{H}\Psi(r, R) = E\Psi(r, R), \quad (2.1)$$

where \hat{H} is the many-body Hamiltonian, Ψ the many-body wave function, E the eigenenergy of the many-body state Ψ and r and R are collective coordinates which encode the coordinates of all electrons and nuclei, respectively. In this general form the

Schrödinger equation has $3(N_{\text{I}}+N_{\text{el}})$ degrees of freedom with N_{I} and N_{el} being the number of nuclei and electrons, respectively. Since it is not exactly solvable, the first major approximation introduced is the adiabatic Born–Oppenheimer approximation (BOA). It separates the electronic and nuclei degrees of freedom by stating that the many-body wave function $\Psi(r, R)$ is a superposition of the many-electron wave function $\psi_{\nu}(r; R)$ and many-nuclei wave function $\chi_{\nu}(R)$, expressed by:[22]

$$\Psi(r, R) = \sum_{\nu} \psi_{\nu}(r; R)\chi_{\nu}(R). \quad (2.2)$$

Here, ν is the state of the electronic sub-system. In the approximation it is assumed that the electrons follow the motion of the nuclei adiabatically in absence of any type of energy exchange by scattering processes. That seems to be a rather crude approximation at first glance, but for the investigation of the ground-state (GS) of the system in the zero temperature limit, it is appropriate to reduce the complexity of the problem to $3N_{\text{el}}$ degrees of freedom. By plugging the Ansatz of Eq. 2.2 into Eq. 2.1, the Schrödinger equation of the many-electron system is obtained:

$$\hat{H}_{\text{el}}\psi_{\nu}(r; R) = E_{\nu}\psi_{\nu}(r; R), \quad (2.3)$$

with the electronic Hamiltonian given by:

$$\hat{H}_{\text{el}} = \hat{T}_{\text{e}} + \hat{V}_{\text{ee}} + \hat{V}_{\text{en}}, \quad (2.4)$$

where \hat{T}_{e} and \hat{V}_{ee} are the kinetic energy and the electron-electron interaction, respectively. \hat{V}_{en} is the external potential acting on the electrons created by the nuclei. The dependence of the many-electron wave function $\psi_{\nu}(r; R)$ on R is parametric. The most troubling term in this equation is the Coulomb (potential) interaction between the electrons \hat{V}_{ee} , since it is accompanied by a double sum over all electrons and dependent on two-particle coordinates:

$$\hat{V}_{\text{ee}} = \sum_{\substack{i,j=1 \\ i \neq j}}^{N_{\text{el}}} \frac{1}{|\hat{\mathbf{r}}_i - \hat{\mathbf{r}}_j|}. \quad (2.5)$$

For practical reasons, all formulas in this chapter are given in Hartree atomic units (a.u.), in which the reduced Planck's constant \hbar , the electronic mass m , the elementary charge squared e^2 as well as Coulomb constant $k_{\text{e}} = \frac{1}{4\pi\epsilon_0}$ are equal to one ($\hbar = m = e^2 = k_{\text{e}} = 1$). In spite of the simplifications, the computational costs of the many-electron Schrödinger equation 2.3 still increases *exponentially* with the number of electrons N_{el} and quickly becomes too large to compute for any real system. In the 1960s, Hohenberg, Kohn and Sham [19, 23] developed a method that reduced the computational effort to a linear factor scaling with the number of electrons. This was achieved by establishing a one-to-one correspondence between the ground-state wave function of the many-body system ψ_{GS} and the electron density n . The density operator of a N_{el} -electron system is

defined by:[24]

$$\hat{n}(\mathbf{r}) = \sum_{i=1}^{N_{\text{el}}} \delta(\mathbf{r} - \hat{\mathbf{r}}_i), \quad (2.6)$$

representing the electron density by delta functions, with $\hat{\mathbf{r}}_i$ being the particle position operators. Using this definition the external potential created by the nuclei can be written as:

$$\langle \psi | \hat{V}_{\text{en}} | \psi \rangle = \int v_{\text{en}}(\mathbf{r}; R) n(\mathbf{r}) d\mathbf{r}. \quad (2.7)$$

Since \hat{V}_{en} is the only term depend on the nuclear coordinates R , it encodes the quantum mechanical properties of the system, resulting in a one-to-one correspondence with the electronic Hamiltonian \hat{H}_{el} and the ground-state wave function ψ_{GS} .

That \hat{V}_{en} is a unique functional of the ground-state electron density $n_{\text{GS}}(\mathbf{r})$ is the insight of the first Hohenberg-Kohn theorem. In other words, for each \hat{V}_{en} there is only one corresponding electron density $n(\mathbf{r})$. The consequence of the theorem is that any quantity expressed by a functional of the ground-state electron wave function may also be expressed as a functional of the electron density. The ground-state energy of the system for instance can be written as:[23]

$$E[n] = F[n] + \int v_{\text{en}}(\mathbf{r}; R) n(\mathbf{r}) d\mathbf{r}, \quad (2.8)$$

where $F[n]$ is the density functional given by:

$$F[n] = \langle \psi | \hat{T}_{\text{e}} + \hat{V}_{\text{ee}} | \psi \rangle. \quad (2.9)$$

Since \hat{T}_{e} and \hat{V}_{ee} only depend on the number of electrons (but not on the nuclear coordinates) $F[n]$ is a universal functional of the density n . Applying the variational principle to eq. 2.8 (under the condition of the minimization of the density $n(\mathbf{r})$) Hohenberg and Kohn proved that the total energy $E[n]$ is minimized at the (N -electron) ground-state density $n_{\text{GS}}(\mathbf{r})$, which came to be known as the second Hohenberg-Kohn theorem.

At this point, however, $F[n]$ remains unknown due to missing information about the ground-state wave function in kinetic energy T_{e} and the density in the external potential V_{en} . In 1965 Kohn and Sham proposed a method to reformulate the problem. The approach recasts the many-body Schrödinger equation into a set of single-particle equations subject to a single-particle potential v_{KS} called Kohn-Sham (KS) potential:[25]

$$v_{\text{KS}}(\mathbf{r}, [n]) = v_{\text{en}}(\mathbf{r}) + v_{\text{H}}(\mathbf{r}) + v_{\text{xc}}(\mathbf{r}, [n]), \quad (2.10)$$

where $v_{\text{xc}}(\mathbf{r}, [n])$ is the single-particle exchange-correlation potential related to the

exchange-correlation energy by the variational principle:

$$v_{\text{xc}}(\mathbf{r}, [n]) = \frac{\delta E_{\text{XC}}[n]}{\delta n} \quad (2.11)$$

and $v_{\text{H}}(\mathbf{r})$ is the Hartree potential given by the integration of the electron density $n(\mathbf{r}')$ divided by the distance $|\mathbf{r} - \mathbf{r}'|$ over real space:

$$v_{\text{H}}(\mathbf{r}) = \int d\mathbf{r}' \frac{n(\mathbf{r}')}{|\mathbf{r} - \mathbf{r}'|}. \quad (2.12)$$

The Hartree potential resembles the direct interaction between the electrons mediated by the Coulomb force. To account for the full interaction between the electrons without scattering events an additional indirect term is needed, which is incorporated in the exchange part of $v_{\text{xc}}(\mathbf{r}, [n])$. Now Kohn and Sham showed that the ground-state electron density $n_{\text{GS}}(\mathbf{r})$ of a real interacting system coincides with the electron density of an auxiliary single-particle non-interacting system in the local external potential $v_{\text{KS}}(\mathbf{r}, [n])$. A physical intuition that supports this claim without providing a mathematical proof is the unique relation between the external potential \hat{V}_{en} and the electron Hamiltonian \hat{H}_{e} .

The reduction of the Hamiltonian operator \hat{H}_{KS} to a simple sum of single-particle operators h_i^{KS} makes the key difference in this approach. The single-particle Schrödinger equation, known as the KS equation, obtained by this considerations, is given by:[19]

$$\left[-\frac{\nabla^2}{2} + v_{\text{KS}}(\mathbf{r}, [n]) \right] \varphi_i^{\text{KS}}(\mathbf{r}) = \varepsilon_i^{\text{KS}} \varphi_i^{\text{KS}}(\mathbf{r}), \quad (2.13)$$

where $\varphi_i^{\text{KS}}(\mathbf{r})$ and $\varepsilon_i^{\text{KS}}$ are the KS orbitals and energies, respectively. Eq. 2.13 must be solved iteratively with the expression for the ground-state electron density given by:

$$n_{\text{GS}}(\mathbf{r}) = \sum_{i=1}^N |\varphi_i^{\text{KS}}(\mathbf{r})|^2. \quad (2.14)$$

Together the equations 2.10; 2.13 and 2.14 form a set of self-consistent equations yielding the exact electron density of the true ground-state system. But since the exchange-correlation potential $v_{\text{xc}}(\mathbf{r}, [n])$ is unknown analytically, it needs to be approximated, for example by quantum Monte Carlo simulations. The iterative solving procedure is depicted in Fig. 2.1. First, an educated initial guess of the electron density $\tilde{n}(\mathbf{r})$ is made. With that density the KS potential and equation are solved, obtaining the KS single particle orbitals $\varphi_i^{\text{KS}}(\mathbf{r})$. These are then used to calculate a new electron density $n(\mathbf{r})$. If this density $n(\mathbf{r})$ is equal to $\tilde{n}(\mathbf{r})$ the self-consistent loop is closed and the density is put out. If they are unequal the density is updated and the loop repeated until the densities are self-consistent.

However, the approximate nature of the exchange-correlation potential is not yet taken into account and influences the accuracy of the calculated electron density. The most well-known approximations are the local density approximation (LDA) [26] and the

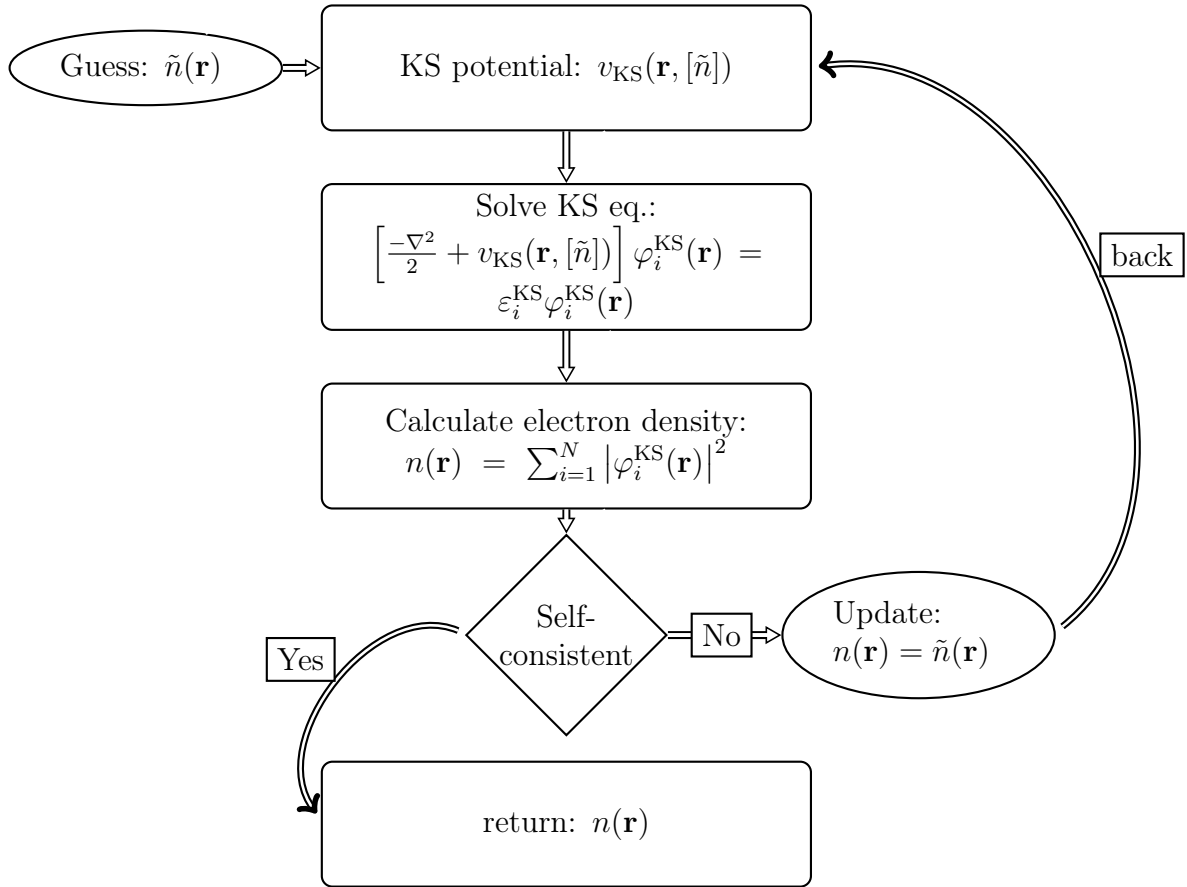


Figure 2.1.: Flow diagram to solve the Kohn-Sham equation.

generalized gradient approximation (GGA) [27]. In the LDA the homogeneous electron gas (HEG) model is used to approximate the exchange-correlation energy. The HEG model describes a system of interacting electrons with a homogeneous positively-charge background (jellium) keeping the system neutral and will be discussed in greater detail in section 2.2.1. When the model is applied, the exchange part of $v_{\text{xc}}(\mathbf{r}, [n])$ can be formulated as an analytic expression of the exchange energy per particle as a functional of the electron density given by:

$$\epsilon_{\text{x}}^{\text{LDA}}[n] = -\frac{3}{4} \left(\frac{3}{\pi}\right)^{\frac{1}{3}} n(\mathbf{r})^{\frac{1}{3}}. \quad (2.15)$$

In that approximation, the correlation energy is obtained by quantum Monte Carlo methods and the interpolation of the exact high- and low-density limits. The accuracy of the LDA for metals and sp-bonded semiconductors is already quite impressive, but for systems with highly-localised electronic states, such as d - and f -electron systems, it is not accurate, since they tend to exhibit inhomogeneities in the density. Problems of the LDA are *inter alia* no consideration of the van der Waals interactions. Overall it is

a good, but not a perfect approximation.

An appropriate step beyond the LDA is the gradient expansion of the density, already suggested by Hohenberg and Kohn 1964. [23] In that model the electron density $n(\mathbf{r})$ is given by a uniform part \bar{n} and a weak and slowly varying density modulation $\delta n(\mathbf{r})$ in space ($n(\mathbf{r}) = \bar{n} + \delta n(\mathbf{r})$). A concrete formulation of the GGA based on this gradient approach was first achieved in 1980 by Perdew and Langreth [28] and was later optimized by Perdew, Burke and Ernzerhof (PBE) [29]. In addition, a wide range of GGAs have been formulated over the years [30]. The general form of the exchange-correlation energy functional in these GGAs takes the following:

$$E_{xc}^{\text{GGA}}[n_{\uparrow}, n_{\downarrow}] = \int d\mathbf{r} f(n_{\uparrow}(\mathbf{r}), n_{\downarrow}(\mathbf{r}), \nabla n_{\uparrow}(\mathbf{r}), \nabla n_{\downarrow}(\mathbf{r})), \quad (2.16)$$

with \uparrow and \downarrow indicating the spin of the electron density. The function f in this equation takes several forms depending on the GGA. In the GGA a real space cutoff is employed to assure the physicality of the approximation by reinstating the correct sum rules and the right properties of the system. In the derivation by PBE, f is entirely expressed through fundamental constants. The strength of the GGA lies in the description of molecules and their dissociation energies and in some cases the overestimation of the binding energies in the LDA is reduced by a factor of 5. A comparison between the dissociation energies of selected number of molecules in the LDA and GGA is shown in Tab. 2.1.

Molecule	ΔE^{LDA}	ΔE^{GGA}	ΔE^{exp}
H ₂	4.90	4.55	4.73
LiH	2.60	2.25	2.51
CH ₄	20.0	18.2	18.2
NH ₃	14.6	13.1	12.9
OH	5.38	4.77	4.64
H ₂ O	11.6	10.15	10.06
N ₂	11.6	10.5	9.93
O ₂	7.59	6.24	5.25
F ₂	3.38	2.30	1.69

Table 2.1.: Energies for the dissociation of molecules in eV.[29]

2.1.2. Numerical methods

The focus of the discussion up to this point has been the isolated electronic system. Since the systems under consideration are extended solids, the number of electrons and nuclei approaches the Avogadro number. But their periodicity can be used to reduce

the problem to a single unit cell in most cases. This is achieved by exploiting the translational symmetry within the crystalline solids, so that the periodic KS-potential is the same upon shifts by the lattice vector \mathbf{R} ($v_{\text{KS}}(\mathbf{r}) = v_{\text{KS}}(\mathbf{r} + \mathbf{R})$). According to Bloch's theorem [31] the eigenfunctions solving these single-particle Schrödinger equations, such as the KS-equation 2.13, are given by Bloch wavefunction of the form:

$$\psi_{n,\mathbf{k}}(\mathbf{r}) = \frac{1}{\sqrt{N_p}} u_{n,\mathbf{k}}(\mathbf{r}) e^{i\mathbf{k}\cdot\mathbf{r}}, \quad (2.17)$$

where n denotes the band index, \mathbf{k} the momentum within the first Brillouin zone (BZ), N_p the number of the unit cell and $u_{n,\mathbf{k}}(\mathbf{r})$ a periodic function with the same periodicity as the crystal lattice. Due to its periodicity, it is sufficient to study the most compact primitive cell of the lattice, the first BZ, using Born-von-Karman (BvK) boundary conditions. They allow the treatment of an extended periodic system by a BvK supercell that is constructed out of multiple unit cells, with the reciprocal volume of the system given by $\Omega = N_p \Omega_p$. Since any periodic function can be expanded as a Fourier series, the eigenfunction can be written as:

$$\psi_{n,\mathbf{k}}(\mathbf{r}) = \frac{1}{\sqrt{N_p \Omega_p}} \sum_{\mathbf{G}} c_{n,\mathbf{k}}(\mathbf{G}) e^{i(\mathbf{k} + \mathbf{G})\cdot\mathbf{r}}, \quad (2.18)$$

with the reciprocal lattice vector \mathbf{G} and the plane-wave coefficients $c_{n,\mathbf{k}}(\mathbf{G})$. Note that the eigenfunction described in Eq. 2.18 is taken for a specific band n and momentum \mathbf{k} . In computation, these states $\psi_{n,\mathbf{k}}(\mathbf{r})$ are calculated for a finite number of \mathbf{k} -points given a discrete set of eigenstates. Intrinsic properties of the crystal given in “per unit cell” are averaged over the sum of \mathbf{k} divided by the number of \mathbf{k} -points. In the limit of infinitely many \mathbf{k} -points, the grid becomes a dense continuum and the eigenvalues $\varepsilon_{n,\mathbf{k}}$ become continuous bands.

Using the plane-wave coefficients $c_{n,\mathbf{k}}(\mathbf{G})$ the KS equation 2.13 in the plane wave expansion can be expressed in reciprocal space:[30]

$$\sum_{\mathbf{G}'} \left[\frac{|\mathbf{k} + \mathbf{G}'|^2}{2} \delta_{\mathbf{G},\mathbf{G}'} + v_{\text{KS}}[n](\mathbf{G} - \mathbf{G}') \right] c_{n,\mathbf{k}}(\mathbf{G}') = \varepsilon_{n,\mathbf{k}} c_{n,\mathbf{k}}(\mathbf{G}) \quad (2.19)$$

Due to computational limitations, the number of \mathbf{G} vectors considered in the calculation needs to be truncated using a kinetic energy cutoff:[32]

$$\frac{|\mathbf{k} + \mathbf{G}|^2}{2} \leq E_{\text{cut}} \quad (2.20)$$

That way only \mathbf{G} vectors evaluated for each \mathbf{k} -point below a certain kinetic energy cutoff are considered in the series. The higher Fourier components are neglected, making a preliminary investigation of this parameter by convergence tests necessary (in any plane wave code).

The plane wave method of the KS equation 2.19 enables a conveniently simple frame-

work to describe the eigenfunctions, while they are smooth (and slowly varying). However, to treat the core electrons near the atomic nuclei correctly, a large number of Fourier components would be required, because the eigenfunctions exhibit nodes in that region. Since the core electrons are bound to the atomic nuclei and therefore chemically inert, they do not contribute much to the physical and chemical properties of materials. It is reasonable to describe them together with the nuclei using a (so-called) pseudopotential (PP), in which the core electrons are fixed and the bare nuclei potential is replaced by a screened effective potential. Together with the plane wave formalism, this concept made the calculation of material properties affordable and is the reason why they are so popular today. [33] There has been much development in the construction of PPs, from empirical screened PPs [34] to modern self-consistently screened *ab-initio* ones [35].

An important feature of useful PPs is their transferability. An ideal pseudopotential of an element would be able to describe a single atom, molecular arrangements, as well as its solid state form in a compound (bulk crystals) [36]. But there are limits in their description of the all-electron wavefunction (including the core electrons). Since the PP is supposed to be smooth it should not have any nodes, which lead to wiggles in the pseudo-wavefunction. In real space, the outermost node of the wave-function is therefore the natural limit of approximation. To reach this limit as closely as possible an ionic cutoff radius r_c is introduced. Outside this cutoff, the pseudo-wavefunction and the all-electron wavefunction should coincide, while inside the pseudo-wavefunction is smooth.

A class of widely used pseudopotentials are called norm-conserving potentials. Although the wavefunctions inside the ionic cutoff radius are not the same, the charge they enclose must be equal, leading to the condition that their norm must be conserved even within the radius r_c : [37]

$$\int_0^{r_c} dr |u_{nl}^{\text{PP}}(r; \varepsilon_{nl}^{\text{PP}})|^2 = \int_0^{r_c} dr |u_{nl}^{\text{AE}}(r; \varepsilon_{nl})|^2. \quad (2.21)$$

This condition is imposed for the radial wavefunctions leading to replacement of vectorial momentum \mathbf{k} by the quantum number l of the angular momentum. PP and AE indicate the association to the pseudopotential and all-electron, respectively. A last (and obvious) requirement is that the valence AE and PP eigenvalues must be equal ($\varepsilon_{nl}^{\text{PP}} = \varepsilon_{nl}^{\text{AE}}$). The use of radial wavefunctions in the context of electron structure calculations is the approximation and simplification that the screening (of the nuclei) is spherical, which leads to the formulation of the radial KS equation:[19]

$$\left[-\frac{1}{2} \frac{d^2}{dr^2} + \frac{l(l+1)}{2r^2} + v(r, [\rho]) - \varepsilon_{nl} \right] (ru_{nl}(r)) = 0. \quad (2.22)$$

Together with the equation for the one-electron potential:

$$v(r, [\rho]) = -\frac{N_Z}{r} + v_{\text{H}}(r, [\rho]) + v_{\text{xc}}(r, [\rho]), \quad (2.23)$$

and the radial electron density:[5]

$$\rho(r) = \frac{1}{4\pi} \sum_{n \in \text{occ}} \sum_{l=0}^{n-1} f_{nl} \left| \frac{u_{nl}(r; \varepsilon_{nl})}{r} \right|^2. \quad (2.24)$$

the radial KS equation 2.22 builds a set of self-consistently solvable equations. Here, N_Z is the number of elementary charges of the nucleus and f_{nl} the probability of finding an electron in the state n, l given by the Fermi-Dirac distribution. To obtain a smooth transition at r_{cut} the logarithmic derivatives and the first energy derivatives of the logarithmic derivatives of the all-electron and pseudo wavefunctions must agree. Further work dealing with muffin-tin spheres and linear augmented planewaves (LAPW) is detailed in [30, 32, 33, 35].

2.2. Interacting systems and excited states

Interacting particle systems and excited states are quantum many-body problems and need to be treated in a suited framework. They arise from many-particle interactions and depending on the types of excitation different formalism's and approximations are useful to approach them. For the description of the polarization of a medium and collective behaviour of electron gas, the dielectric function in the so-called RPA is quite convincing. In this section a derivation of this quantity from the general response function is sketched.

2.2.1. RPA dielectric function and plasmons

The dielectric function is a complex object describing the dielectric response of a material to perturbations, e.g., the interaction with light. It includes information about the polarization of the medium due to external, but also internal excitations. Knowledge of the full dielectric function enables the understanding of the electronic system and its response to perturbations.

The coupling of a time-dependent external potential, for example an electric field, to the electron gas can be expressed in the following way:

$$\int V_{\text{ext}}(\mathbf{r}, t) \hat{n}(\mathbf{r}) d\mathbf{r}, \quad (2.25)$$

with $\hat{n}(\mathbf{r})$ being the electron density operator introduced in Eq.2.6. This external potential sets in after a initial time t_0 , and it is assumed that the system is in the ground state beforehand. For small field strengths it is sufficient enough to evaluate the linear response of the system leading to a polarization that is proportional to the field strength. The unitary time-evolution operator corresponding to this linear response theory is given

by:[24]

$$\hat{U}_1(t, t_0) = e^{-i\hat{H}(t, t_0)} \left[\hat{1} - i \int_{t_0}^t \hat{B}(t' - t_0) F(t') dt' \right]. \quad (2.26)$$

Where $\hat{H}(t, t_0)$ is the Hamiltonian of the system and $\hat{B}(t' - t_0)$ corresponds to $\hat{n}(\mathbf{r})$ and $F(t')$ to $V_{ext}(\mathbf{r}, t)$ in first order. The repercussion of the perturbation can be described by the *retarded* linear response function:

$$\chi_{AB}(\tau) = -i\Theta(\tau)\langle[\hat{A}(\tau), \hat{B}]_0\rangle. \quad (2.27)$$

Here, \hat{A} and \hat{B} are time-dependented operators under the influence of the after-effect of the perturbation at times $\tau \equiv t - t' > 0$. $[\hat{A}, \hat{B}]$ is the commutator of the two operators and $\langle \dots \rangle_0$ the average of the equilibrium of the system. The Heaviside step function $\Theta(\tau)$ is zero for $\tau < 0$ and $\tau > 1$. $\chi_{AB}(\tau)$ is called *retarded* or also *causal* since it describes the after-effect of the perturbation ensured by $\Theta(\tau)$. In the description of the exact eigenstates $|\psi_n\rangle$ the Fourier transform, known as the Lehman representation, of the response function takes to form:[24]

$$\chi_{AB}(\omega) = \sum_{nm} \frac{P_m - P_n}{\omega - \omega_{nm} + i\eta} A_{mn} B_{nm}, \quad (2.28)$$

with a positive infinitesimal $\eta \rightarrow 0^+$ and the population probability:

$$P_n = \frac{e^{-\beta E_n}}{Z}, \quad (2.29)$$

where $\beta = 1/(k_B T)$ is the inverse thermal energy and $Z = \sum_n e^{-\beta E_n}$ is the canonical partition function. In the zero-temperature limit the population probability is equal to one ($P_n = 1$) in the ground-state (at $n = 0$), while all the other states are zero ($P_n = 0$). In the complex plain $\chi_{AB}(\omega)$ is analytic in the upper part and exhibits simple poles in the lower half of the equation. Further specifying Eq. 2.28 one can express the density-density response function in a periodic potential by:

$$\chi_{nn}(\mathbf{q}, \omega) = \frac{1}{V} \chi_{n_{\mathbf{q}} n_{-\mathbf{q}}}(\omega) = \frac{1}{V} \sum_{nm} \frac{P_m - P_n}{\omega - \omega_{nm} + i\eta} |(\hat{n}_{\mathbf{q}})_{nm}|^2. \quad (2.30)$$

Where the density fluctuation operator at the wave vector \mathbf{q} is given by:

$$\hat{n}_{\mathbf{q}} = \sum_j e^{-i\mathbf{q}\mathbf{r}_j}, \quad (2.31)$$

and V being the volume of the system under consideration. In the non-interacting

electron picture this density-density response function can be written as:

$$\chi_0(\mathbf{q}, \omega) = \frac{1}{V} \sum_{\mathbf{k}} \frac{n_{\mathbf{k}-\mathbf{k}+\mathbf{q}}}{\omega + \varepsilon_{\mathbf{k}} - \varepsilon_{\mathbf{k}+\mathbf{q}} + i\eta}, \quad (2.32)$$

In the denominator of the equation there is no sign of energy loss due to scattering and excitation events since the electrons are independent, which is expressed by the zero in the subscript of the χ and the spin orientation is neglected. Eq. 2.32 is also called the Lindhard function, which becomes purely real in its static limit ($\omega = 0$) since the denominator only vanishes simultaneously with the nominator the positive infinitesimal η is not required any more.

On the basis of this independent electron model, the interacting electron liquid can now be described. The linear response function of the interacting system enables the understanding of various many-body phenomena like screening effects, collective (mode) excitations and quasiparticle properties, e.g., effective masses.

A prominent property is the screening of an additional coulomb field V_{ind} for example created by an impurity of an external fast-moving electron. The screened scalar potential W resulting from such a perturbation is given by the summation of the external field V_{ext} and the induced field V_{ind} , which takes the form of a Hartree potential (see Eq. 2.12) with the electron density being replaced by a time-dependent induced density $n_{\text{ind}}(\mathbf{r}, t) = n(\mathbf{r}, t) - n(\mathbf{r})$. The screened scalar potential W can be expressed in terms of the dielectric function ϵ as well. In the case of the HEG their relation is:

$$W(\mathbf{q}, \omega) = \frac{V_{\text{ext}}}{\epsilon(\mathbf{q}, \omega)}. \quad (2.33)$$

In the case of V_{ext} representing the bare Coulomb interaction $v_{\mathbf{q}}$, $W(\mathbf{q}, \omega)$ would therefore be the screened Coulomb interaction. The dielectric function $\epsilon(\mathbf{q}, \omega)$ is closely related to the density-density response function $\chi_{nn}(\mathbf{q}, \omega)$ and incorporates the induced field V_{ind} . Since the dielectric function is an observable (measurable by experiment), as the electron density, there is a high interest in its exact theoretical description and the approximations enabling its calculations (from first-principle). A very successful approximation is the RPA, since it properly describes the emergence and collective behaviour of plasmons. The dynamic dielectric function in the RPA is given by:

$$\epsilon^{\text{RPA}}(\mathbf{q}, \omega) = 1 - v_{\mathbf{q}}\chi_0(\mathbf{q}, \omega). \quad (2.34)$$

The most intuitive way of explaining the RPA is a diagram technique of the interactions taking place in a medium. In Fig. 2.2(a) the so-called Feynman diagram of a single-fermion closed loop is presented. The wiggly lines represent the Coulomb interaction while the vertex with the arrows is a polarization bubble. The point at which the left wiggly line meets the bubble depicts a scattering event in which an electron-hole pair is created. The upper part of the bubble features the propagation of the electron, while the lower part features the propagation of the hole, respectively. The point at which the right wiggly line starts at the bubble depicts the annihilation of the electron-hole pair. The

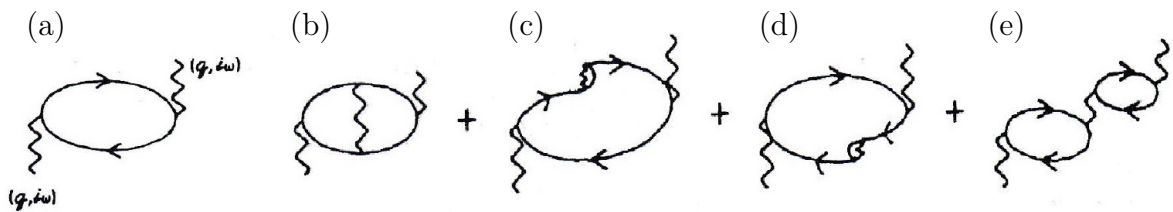


Figure 2.2.: Feynman diagrams of single- and double-fermion closed loops. The wiggly lines represent the Coulomb interaction while the vertex with the arrows are polarization bubbles.[6]

vertex is called polarization bubble since it describes the polarization of the medium by the electron-hole pair. Many more excitation processes in the medium could be imagined such as those shown in Fig. 5.10. The interaction diagrams depicted in that figure describe multi scattering events. Fig. 2.2(b) is similar to Fig. 2.2(a) with the difference that an interaction is taking place between the electron and the hole. Fig. 2.2(c+d) are exchange energy diagrams that are related to the self-energy of the (virtual) particles created during the polarization. The last Fig 2.2(e) is a continuation of the single polarization bubble of Fig 2.2(a) with two bubbles and the Coulomb interaction line between them. Hence it is a repetition of the single bubble polarization diagram. The RPA is the summation of all single bubble polarization diagrams, neglecting the other multi scattering events (like the ones presented in Fig. 2.2(b-e)) and leads to Eq. 2.34, which includes electron-hole interaction. As already mentioned, the most distinctive property of RPA is the description of charge-density fluctuations by collective bosonic excitations. The plasmons thus arise from the interacting electron liquid. Their dispersion and the electron-hole excitation in the HEG case can be illustrated using the loss function:[38]

$$L(\mathbf{q}, \omega) = \text{Im } \epsilon_{\text{RPA}}^{-1}(\mathbf{q}, \omega) \quad (2.35)$$

The HEG model provides a convenient way to phenomenologically understand the satellite features appearing in the spectral function of the photoemission measurements . It denotes a system of electrons interacting with a homogeneous positively background, that maintains charge neutrality. The electronic correlation between electrons and plasmons is treated via an independent boson model, which can be precisely determined for a localized electron interacting with a plasmon bath. [39]

The loss function arising from this model is presented in Fig. 2.3. Here the energy and momentum are given in units of the plasmon energy ω_{pl} and the Fermi momentum k_{F} . The loss function describes the possible energy transfer of the electrons through band transitions. The parabolic nature of the model is recognisable because the momentum transfer of $\sim 2k_{\text{F}}$ takes this form towards higher energies. It represents electron-hole excitations within the band. The interesting feature of the plot is the small band at the plasmon energy, which describes an energy transfer of ω_{pl} without momentum being transferred corresponding to a vertical interband transition of an electron in the band model. This energy transfer leads to the formation of a plasmonic polaron band red-shifted by the plasmon energy. The condition for its emergence follows from the dielectric

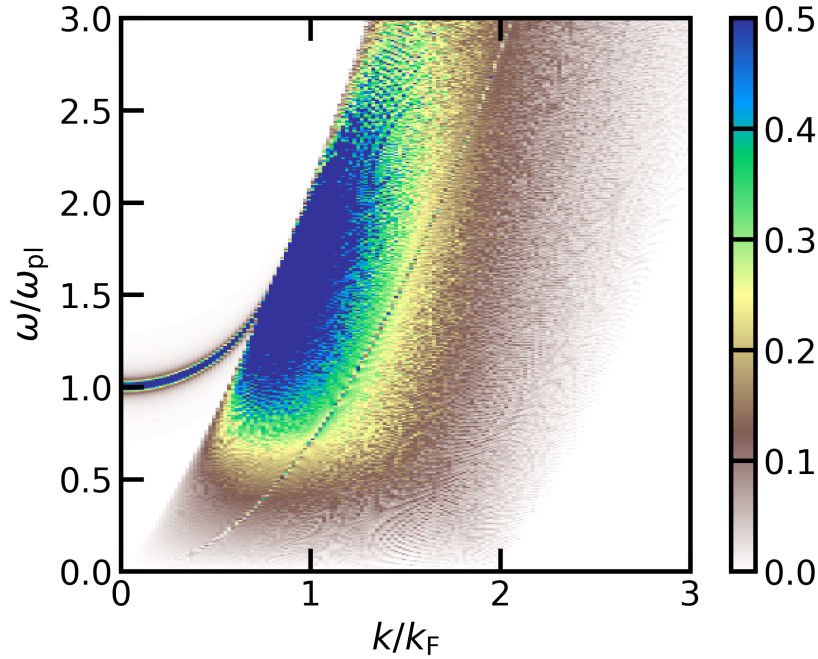


Figure 2.3.: Loss function of the homogeneous electron gas calculated for a Wigner-Seitz radius of $r_s = 22$ a.u. corresponding to a free electron density of $n = 1.475 \cdot 10^{20} \text{ cm}^{-3}$. The energy (momentum) is given in units of the plasmon energy ω_{pl} (Fermi momentum k_F), respectively.

function being equal to zero ($\epsilon[\mathbf{q}, \omega_{\text{pl}}(\mathbf{q})] = 0$). For momenta ($\mathbf{q} = 0$) in this condition, the plasmon frequency can be obtained. In the HEG model it is given by:

$$\omega_{\text{pl}}^{\text{HEG}} = \sqrt{\frac{4\pi n}{m}}, \quad (2.36)$$

with the electron density n and the electron mass m .

Since the electrons in the conduction band of n-typed doped semiconductors can be considered as nearly free particles with a modified effective mass and a screened Coulomb interaction, due to the presents of further charge carriers, the consideration of the HEG is useful as a basis for the treatment of conduction band electrons.

2.2.2. Computation of the electron-boson coupling

The Hamiltonian describing electron-boson interaction is given by:[6]

$$\hat{H}^{\text{e-b}} = \sum_{nm\nu} \sum_{\mathbf{k}, \mathbf{q}} g_{nm\nu}^{\text{e-b}}(\mathbf{k}, \mathbf{q}) \hat{c}_{m\mathbf{k}+\mathbf{q}}^\dagger \hat{c}_{n\mathbf{k}} (\hat{b}_{\mathbf{q}\nu} + \hat{b}_{-\mathbf{q}\nu}^\dagger), \quad (2.37)$$

with the band indices n and m , the bosonic modes ν and the electron \mathbf{k} and boson \mathbf{q} momenta. $g_{nm\nu}^{\text{e-b}}(\mathbf{k}, \mathbf{q})$ denotes the electron-boson coupling matrix elements, $\hat{c}_{m\mathbf{k}+\mathbf{q}}^\dagger$ and $\hat{c}_{n\mathbf{k}}$ the electronic (fermionic) and $\hat{b}_{-\mathbf{q}\nu}^\dagger$ and $\hat{b}_{\mathbf{q}\nu}$ the bosonic creation and annihilation operators. In the notation of the second quantisation, they allow a simpler formulation of

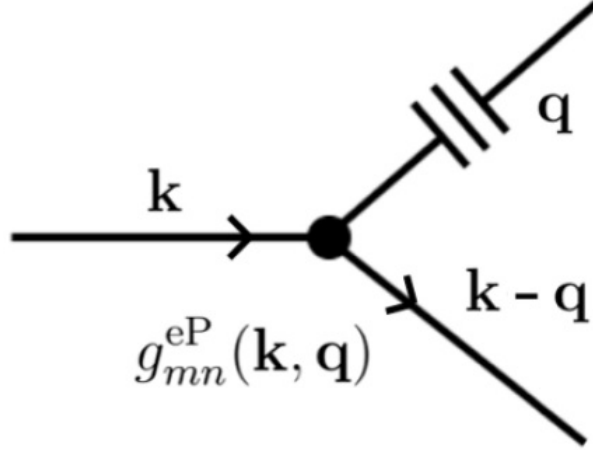


Figure 2.4.: Diagrammatic representation of the electron-plasmon scattering process.[4]

the Hamiltonian and stand for the creation or annihilation of a particle in a specific state and with a certain momentum. Using many-body perturbation theory the electron-boson self-energy can be calculated. In the so-called Fan-Migdal approximation the electron-boson self-energy takes the form:[3]

$$\Sigma_{nk}^{e-b} = \int \frac{d\mathbf{q}}{\Omega_{\text{BZ}}} \sum_{m\nu} |g_{mn\nu}^{e-b}(\mathbf{k}, \mathbf{q})|^2 \left[\frac{n_{\mathbf{q}\nu} + f_{m\mathbf{k}+\mathbf{q}}}{\varepsilon_{n\mathbf{k}} - \varepsilon_{m\mathbf{k}+\mathbf{q}} + \omega_{\mathbf{q}\nu}^b + i\eta} + \frac{n_{\mathbf{q}\nu} + 1 - f_{m\mathbf{k}+\mathbf{q}}}{\varepsilon_{n\mathbf{k}} - \varepsilon_{m\mathbf{k}+\mathbf{q}} - \omega_{\mathbf{q}\nu}^b + i\eta} \right], \quad (2.38)$$

where Ω_{BZ} is the BZ volume in reciprocal space, m and n are band indices, \mathbf{k} and \mathbf{q} are Bloch wave vectors, n denote the Bose-Einstein and f the Fermi-Dirac distribution, ε are the KS eigenstates, $\omega_{\mathbf{q}\nu}^b$ is the boson frequency and η is a positive infinitesimal. The integral runs over the BZ volume. The first term represents the photoexcitation of an electron via absorption of a boson $+\omega_{\mathbf{q}\nu}^b$, while the second term includes photoholes and the emission of a boson $-\omega_{\mathbf{q}\nu}^b$. The poles of the self-energy, found where the denominator (of the fraction) vanishes, lead to the emergence of additional satellite structures in the spectral function due to bosonic excitations. In the case of electron-plasmon coupling, the ν is dropped since a single plasmon mode is considered which boson frequency corresponds to the plasmon energy $\omega_{\mathbf{q}}^{\text{pl}}$. At this point, the focus of this theory section is put on electron-plasmon coupling, since this type of interaction is typically dominant for high free electron density.[39]

The expression for the electron-plasmon scattering matrix elements in the framework of the GW approximation is given by:[39]

$$g_{mn}^{e-\text{pl}}(\mathbf{k}, \mathbf{q}) = \left[\frac{\partial \varepsilon(\mathbf{q}, \omega)}{\partial \omega} \Big|_{\omega_{\mathbf{q}}^{\text{pl}}} \right]^{-\frac{1}{2}} \left(\frac{4\pi}{\Omega_{\text{BZ}}} \right)^{\frac{1}{2}} \frac{1}{|\mathbf{q}|} \langle \psi_{m\mathbf{k}+\mathbf{q}} | e^{i\mathbf{q}\cdot\mathbf{r}} | \psi_{n\mathbf{k}} \rangle. \quad (2.39)$$

Here, Ω_{BZ} is the BZ volume in reciprocal space, ε is the dielectric function in de-

pendence on the Bloch wave vector \mathbf{q} and the frequency ω and $\langle \psi_{m\mathbf{k}+\mathbf{q}} | e^{i\mathbf{q}\cdot\mathbf{r}} | \psi_{n\mathbf{k}} \rangle$ gives the transition probability for a scattering process from an initial state $n\mathbf{k}$ to a final state $m\mathbf{k} + \mathbf{q}$. The singularity in electron-plasmon matrix element $\frac{1}{|\mathbf{q}|}$ indicates that the long-wavelength plasmons are dominant in the coupling process.

In Fig. 2.4 the electron-plasmon scattering process characterized by the electron-plasmon scattering matrix element is presented in a diagrammatic way. An electron with the initial momentum \mathbf{k} is scattered into a final state $\mathbf{k} - \mathbf{q}$ while exciting a plasmon with momentum \mathbf{q} in the process.

The tricky part in the computation of Eq. 2.39 is the assessment of the dielectric function, since it requires a rather fine \mathbf{k} -point sampling of the BZ when treating doped materials. To find an approximate description for the matrix coupling elements a parabolic band model for the bottom of the conduction band is introduced. Since the Fermi energy in doped systems is usually located less than 0.1 eV above the conduction band minimum (CBM), this approach is appropriate and allows the total dielectric function of doped systems ϵ^D to be written like:

$$\epsilon^D(\mathbf{q}, \omega) = 1 - v(\mathbf{q})[\chi^I(\mathbf{q}, \omega) + \chi^{\text{HEG}}(\mathbf{q}, \omega)]. \quad (2.40)$$

Here χ^I is the electron response function of the intrinsic (undoped) system in the framework of the RPA and χ^{HEG} the polarizability of the HEG, which matches the free electron density and effective electron mass of the material in question.

For small (crystal) momenta $\mathbf{q} \rightarrow \mathbf{0}$ the derivative term in Eq. 2.39 can be rewritten to achieve better numerical stability, the transition probability $\langle \psi_{m\mathbf{k}+\mathbf{q}} | e^{i\mathbf{q}\cdot\mathbf{r}} | \psi_{n\mathbf{k}} \rangle$ can be approximated by a delta function δ_{nm} and the intrinsic dielectric constant approximately equals the high-frequency dielectric function $\epsilon^I(\mathbf{q}, 0) \simeq \epsilon_\infty$. These approximations come at the cost of treating the various bosonic excitations possible in the medium separately, disabling for example the consideration of plasmon-phonon and plasmon-phonon polariton coupling effects. If one wants to look at relaxation processes in a time-resolved manner, this limitation would be more important, but for this work it is sufficient. Using this approximation the electron-plasmon matrix elements can be reformulated by: [9]

$$|g_{mn}^{e\text{-pl}}(\mathbf{k}, \mathbf{q})|^2 = \delta_{nm} \frac{v(\mathbf{q})\omega_{\text{pl}}(\mathbf{q})}{2\Omega_{\text{BZ}}} \left[\frac{1}{\epsilon_\infty - \epsilon^{\text{HEG}}(\mathbf{q}) + 1} - \frac{1}{\epsilon_\infty} \right],$$

with the dielectric function of the HEG in the static Lindhard model [40] is $\epsilon^{\text{HEG}}(\mathbf{q}) = 1 - v(\mathbf{q})\chi^{\text{HEG}}(\mathbf{q}, 0)$. This way the matrix elements can be calculated from first-principle using quantities available from previous computations of the pristine system. To make qualitative comparisons with experiment, the free electron density used in the simulation must reflect the one of the real sample.

2.3. Photoemission signatures of plasmonic polarons

In the theoretical description of photoemission spectra the quasiparticle picture is commonly used, since it refers to effective single-particle states. In this concept a particle, like an electron, is described together with its interaction with the many-body system and

therefore exhibits modified physical properties like a different effective mass or charge. The description of collective excitations, like plasmons and phonons, as quasiparticle can also simplify the computational cost of the many-body problem. The lifetime of these excitations and the quasiparticle behaviour is contained in the imaginary part self-energy, presented in Sec. 2.2.2 for the case of electron-boson coupling. The real part of the self-energy, on the other hand, represents a contribution to the particle's energy due to its interaction with the many-body system.

The quasiparticle concept can be embedded into a Green's function formalism introduced in the later part of this section. The single-particle Green's function can be connected to single-particle excitation spectra obtained by ARPES measurements via the spectral function. First of, the ARPES technique and processing of measured data is discussed, to get a physical intuition for the emission process and the quasiparticle properties the photoemitted electrons exhibit.

2.3.1. Angle-resolved photoemission spectroscopy (technique)

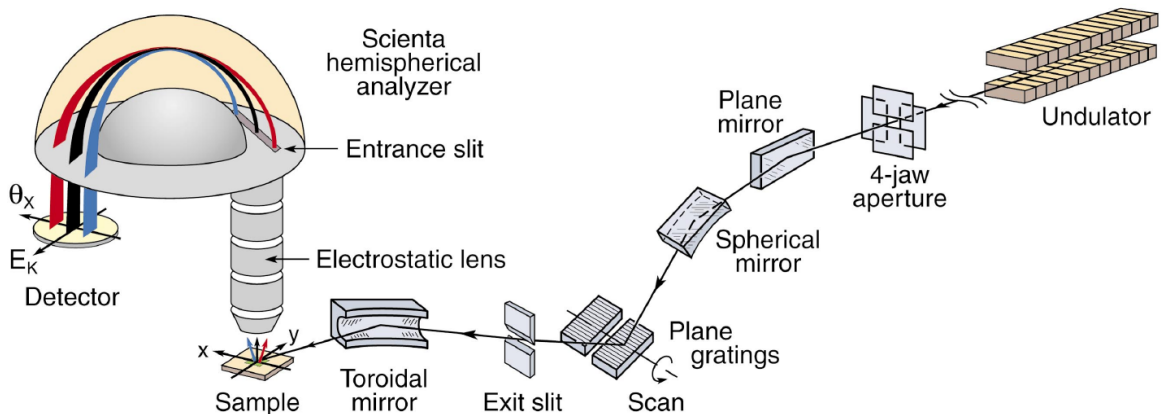


Figure 2.5.: Classical setup of a angle-resolved photoemission spectroscopy experiment including a synchrotron light-source (here an undulator), an assembly of mirror and plane gratings and a hemispherical analyzer.[2]

The classical setup of the ARPES is depicted in Fig 2.5. The highly brilliant, tuneable, polarized and pulsed radiation needed for the measurements is created in a synchrotron light source, for example, an undulator or a free electron laser. In the later, the electrons are forced on a wiggle path leading to a self-induced microbunching of the electrons. Due to the synchronization all electron emit photons of the same energy that entail the positive properties of the light used in the experiment. For the light to end on the sample an assembly of mirrors and lenses is calibrated. The important modification in this step is the monochromatisation of the light by diffraction gratings and the focusing of the beam in size and onto the sample by lenses and slits. The electrons emitted from the sample by the photoelectric effect are focused by an electrostatic lens and enter the hemispherical analyzer by a slit. The analyzer sorts the electrons by their

energy and angular momentum, respectively. After passing the analyser, the electrons end up on a detector, for example a charge-coupled device (CCD) screen. The ARPES measurement technique enables one to directly measure the quasiparticle band structure under the assumption of the sudden approximation, in which the electrons are emitted from the sample instantaneously and encode the information about the excited many-body system. In advanced setups the analyzer along with the detector can be rotated around the sample, or else the sample itself can be rotated. There are also experimental setups with higher data rates that can perform time-of-flight measurements [41].

The photocurrent triggered by the electrons on the detector can be described by the following equation:[42]

$$I_{\text{phot}}(\mathbf{k}_f, E) \propto \sum_i \frac{|\tilde{M}_{fi}|^2}{[\text{Re } k_{f\perp} - k_{i\perp}]^2 + [\text{Im } k_{f\perp}]^2} \delta(\mathbf{k}_{f\parallel} - \mathbf{k}_{i\parallel}) A_i(\mathbf{k}_f, E) f(E). \quad (2.41)$$

Here, i and f are the initial and final states, $f(E)$ is the Fermi-Dirac distribution, $A_i(\mathbf{k}_f, E)$ is the spectral function and \tilde{M}_{fi} are the optical transition dipole matrix elements that are not accounted for by the momentum conservation. The \mathbf{k}_{\parallel} components of the photoelectron momenta are conserved by translation symmetry. But since the perpendicular component $k_{i\perp}$ is not preserved due to a lack of translation symmetry, a quasi-preservation is introduced resulting in an imaginary part in this momentum component. This can be viewed like the imaginary part of the self energy from equation 2.38 in section 2.2.2. The quasi-preservation is achieved via the reformulation of the transition probability for the initial state i to the final state f in the dipol approximation given by $|\langle f | \mathbf{A}_{\text{eff}} \cdot \nabla V_{\text{eff}} | i \rangle|^2 \propto |1/(1 - \exp i(k_{f\perp} - k_{i\perp})a_{\perp})|^2 \propto 1/([\text{Re } k_{f\perp} - k_{i\perp}]^2 + [\text{Im } k_{f\perp}]^2)$, where \mathbf{A}_{eff} is an effective vector potential that contains many-body screening effects and V_{eff} is the effective crystal potential.

Equation 2.41 underlies the fundamental conservation laws of physics for energy and momentum. The basis for the description of photoelectrons and their quantum nature was laid by Einstein in 1905 with the equation for the photoelectric effect given by:[43]

$$E_{\text{kin}} = h\nu - \phi - |E_{\text{B}}|, \quad (2.42)$$

with E_{kin} being the kinetic energy of the electron after the emission process, ϕ denotes the material work function and E_{B} the binding energy. The incident photon energies $h\nu$ used in ARPES experiments are relatively low and lie within the ultraviolet spectrum in the range of 20 – 100 eV. In this energy range, a better energy and pulse resolution is achieved, which comes at the price of a short mean free path length of a few angstroms. [44] That is important to keep in mind for the subtraction of a secondary electron background from the experimental data and to account for the experimental broadening. In subsection 2.3.1 equations to deal with these issues will be introduced.

The momentum conservation of the parallel component \mathbf{k}_{\parallel} can be expressed more specifically by:

$$\mathbf{k}_{i\parallel} = \mathbf{k}_{f\parallel} = \sqrt{\frac{2m}{\hbar^2} E_{\text{kin}}} \sin \vartheta \begin{pmatrix} \cos \varphi \\ \sin \varphi \end{pmatrix}, \quad (2.43)$$

with ϑ and φ being the polar and the azimuth angles of the sample not to be confused with the Θ and Φ the angles of the spectroscopy system. The relation between them is of geometric nature and is given by $\cos \vartheta = \cos \Theta \cos \Phi$ and $\tan \varphi = \sin \Phi / \tan \Theta$. The geometry of the photoemission spectroscopy is schematically shown in Fig. 2.6(a).

The spectral function $A_i(\mathbf{k}, \omega)$ can also be expressed in terms of Fermis golden rule:[2]

$$A_i(\mathbf{k}, \omega = h\nu - E_{\text{kin}}) = \sum_m |\langle \psi_m^{N-1} | c_{\mathbf{k}} | \psi_i^N \rangle|^2 \delta(\omega + E_m^{N-1} - E_i^N). \quad (2.44)$$

Since the photoelectron is removed from the sample the initial N -particle system is left in an excited $(N - 1)$ -particle state m . Thus ψ_i^N is the N -body wave function of the initial state i , $c_{\mathbf{k}}$ is the annihilation operator for the momentum \mathbf{k} and ψ_m^{N-1} the wave function of $(N - 1)$ -body system. Their absolute value squared is the probability for this excitation process (the removal of an electron from the state i and leaving the $(N - 1)$ -particle system in the excited state m).

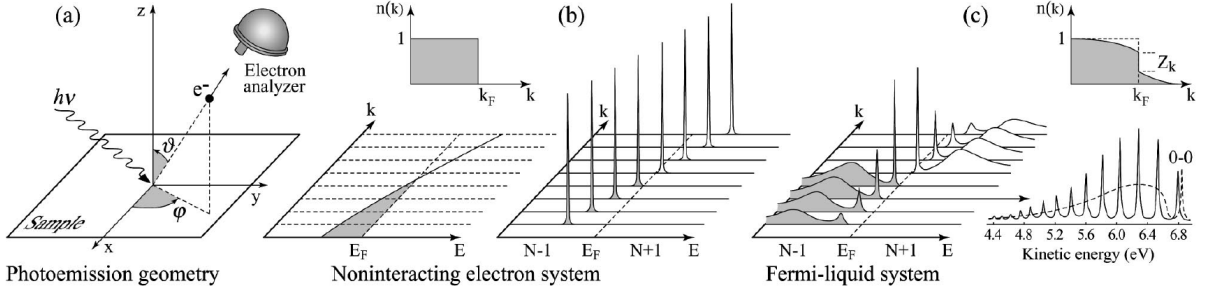


Figure 2.6.: Schematic sketch of the photoemission geometry (a). Spectral function of a noninteracting electron system in the vicinity of the Fermi energy E_F (b). Spectral function of a Fermi-liquid (c) left and photoemission spectrum of gaseous (solid line) and solid (dashed line) hydrogen H_2 (c) right.[2, 45]

In the non-interacting electron picture the electron would be emitted without the system being effected and therefore not being excited. In that picture all of the transition probabilities $|\langle \psi_m^{N-1} | c_{\mathbf{k}} | \psi_i^N \rangle|^2$ will be zero except for the one corresponding to eigenstate m_0 of the N -particle Hamiltonian leading to a collapse of the spectral function to a Dirac delta function of the form $A(\mathbf{k}, \omega) = \delta(\omega + E_{m_0}^{N-1} - E_{m_0}^N)$. The resulting spectral function $A(\mathbf{k}, \omega)$ for different momenta \mathbf{k} is depicted in Fig. 2.6(b). The occupation of the states in that context is given by the Fermi-Dirac distribution in the zero temperature limit. That is, all states until the Fermi energy E_F are filled completely in agreement with the Pauli exclusion principle and all states above that energy are empty.

In the real interacting system, however, multiple transition probabilities $|\langle \psi_m^{N-1} | c_{\mathbf{k}} | \psi_i^N \rangle|^2$ will be different from zero leading to excited states, as shown in Fig. 2.6(c). In the quasiparticle picture it is reasonable as well, since the photoelectron was screened and part of a larger quasiparticle. Upon its removal various higher states corresponding to bosonic excitations like phonons, plasmons and magnons (spin states) can be stimulated depending on their coupling strength to the electron, as discussed in section 2.2.2. These

excitations are reflected by multiple satellite peaks in the spectral function corresponding to the number of excited states m induced during the photoemission process. In the lower right of Fig. 2.6(c) a schematic photoelectron spectrum of molecular hydrogen H_2 is shown. The solid line shows the spectrum of the gaseous phase with a quasiparticle peak at 6.8 eV and several satellite peaks that can be assigned to different vibrational states of the molecule and the dashed line represents the spectrum of solid hydrogen. Due to its more limited rotational and vibrational degrees of freedom, the satellite peaks merge into a continuum. The shift of the quasiparticle peak due to the phase transition can be attributed to a change in the quasiparticle properties, namely its mass.

Secondary electrons and finite-resolution effects

Due to the short mean free path length of the photoelectrons in the crystal there is a probability for inelastic electron scattering that should not be neglected. In these scattering events no collective boson modes are excited, but other electrons in the bands. The scattered electrons have lower energies and are called secondary electrons. They occur inadvertently in photoemission experiment and must be taken into account when analysing the data. A convenient way of doing so for satellites in photoemission spectroscopy is the construction and subtraction of a so-called Shirley background from the measurement data.[46] It is achieved by integrating the measured intrinsic spectral function $\tilde{A}(\omega')$ up to the chemical potential μ : [47]

$$B(\omega) = \int_{\omega}^{\mu} d\omega' \tilde{A}(\omega'),$$

whit $B(\omega)$ is the background of the secondary electrons and subtracting it from the spectral function:

$$A(\omega) = \tilde{A}(\omega) - \beta B(\omega).$$

Here β is a parameter to renormalize the background intensity. This method makes the satellite features more visible and the calculations match the measurements (much) better.

The other issue to be tackled is the finite energy- and momentum-resolution of the experimental setup. It is individual to each ARPES setup and work is ongoing to minimise this error constantly. A possible way to account for this finite-resolution effects is by applying a gaussian-convolution to the calculation in the post-processing of the data. This could, for instance, be achieved using the following equation for the photocurrent $I(\mathbf{k}, \omega)$: [2]

$$\int d\tilde{\omega} M_0(\tilde{\mathbf{k}}, \nu, \mathbf{A}_{\text{eff}}) f(\tilde{\omega}) A(\tilde{\mathbf{k}}, \tilde{\omega}) R(\omega - \tilde{\omega}) Q(\mathbf{k} - \tilde{\mathbf{k}}) + \beta B, \quad (2.45)$$

with $M_0(\tilde{\mathbf{k}}, \nu, \mathbf{A}_{\text{eff}})$ denoting all the optical transition matrix elements including the ones with the momentum conservation. Further $R(\omega - \tilde{\omega})$ is the Gaussian for the energy resolution and $Q(\mathbf{k} - \tilde{\mathbf{k}})$ the distribution function assumed for the momentum solution,

respectively. Since $Q(\mathbf{k} - \tilde{\mathbf{k}})$ is usually more complex than a Gaussian distribution, the finite momentum-resolution is not applied to the calculated data in this thesis.

2.3.2. Spectral function and cumulant expansion

As stated in the beginning of the section, ARPES provides the possibility to gain direct access to the single-particle Green's function of the (N -particle) system. That is why the Green's-function formalism [48] is a powerful approach in the description of photoemission spectra. In the Lehmann representation the *retarded* Green's-function is given by: [6]

$$G(\mathbf{k}, \omega) = \sum_m \frac{|\langle \psi_m^{N-1} | c_{\mathbf{k}} | \psi_i^N \rangle|^2}{\omega + E_m^{N-1} - E_i^N + i\eta} \quad (2.46)$$

The imaginary part of the Green's function is the spectral function $A(\mathbf{k}, \omega) = -(1/\pi) \text{Im} G(\mathbf{k}, \omega)$, which directly relates to the photoelectron current measured in ARPES. The addition of an electron could also be included in Eq. 2.46 by adding a similar fraction with the following denominator $\omega - [E_m^{N+1} - E_i^N] - i\eta$ to the equation corresponding to the inverse photoemission process. In the inverse case, the infinitesimal η is subtracted to resemble an empty band attributed to the *advanced* Green's function. But since standard photoemission is discussed in this thesis the focus is put on the retarded Green's function.

The Green's function is closely related to self-energy $\Sigma(\mathbf{k}, \omega)$ introduced in section 2.2.2. The relation can be expressed in the form of a Dyson's equation:[49]

$$G(\mathbf{k}, \omega) = G^0(\mathbf{k}, \omega) + G^0(\mathbf{k}, \omega)\Sigma(\mathbf{k}, \omega)G(\mathbf{k}, \omega), \quad (2.47)$$

where $G^0(\mathbf{k}, \omega)$ denotes the non-interaction retarded Green's function given by $G^0(\mathbf{k}, \omega) = 1/(\omega - \varepsilon_{\mathbf{k}} + i\eta)$. In real space $G^0(\mathbf{k}, \omega)$ corresponds to the propagation of an electron through the solid without a scattering event taking place. Without this interaction process no energy is dissipated and no other quasiparticles or states are excited. The solution of the Dyson equation yields the exact solution for the Green's function of the interacting system if the self-energy is known exactly, but because of the interdependence of G and Σ , Eq. 2.47 needs to be solved iteratively and self-consistently with the self-energy $\Sigma(\mathbf{k}, \omega)$ in a set of equations introduced by Hedin in 1965 [50].

Due to the relation between Green's function and spectral function, in the diagonal approximation the latter can also be expressed in terms of Fan-Migdal self-energy:[9]

$$A_{n\mathbf{k}}(\omega) = -\frac{1}{\pi} \frac{\text{Im} \Sigma_{n\mathbf{k}}(\omega)}{[\omega - \varepsilon_{n\mathbf{k}} - \text{Re} \Sigma_{n\mathbf{k}}(\omega)]^2 + [\text{Im} \Sigma_{n\mathbf{k}}(\omega)]^2}, \quad (2.48)$$

At the points where the denominator of the fraction becomes zero or has a minimum, a peak occurs in the spectral function. While the real part of the electron self-energy $\text{Re} \Sigma_{n\mathbf{k}}(\omega)$ renormalises the KS eigenenergies $\varepsilon_{n\mathbf{k}}$ leading to a shift of the quasiparticle peak, the imaginary part $\text{Im} \Sigma_{n\mathbf{k}}(\omega)$ is responsible for a Lorentzian broadening of the

peaks due the lifetime effects between the interacting electrons. These lifetime effects are of quasiparticle nature and are given by the rate electrons scatter with thermal plasmons:[3]

$$\Gamma_{n\mathbf{k}} = \tau_{n\mathbf{k}}^{-1} = \frac{2}{\hbar} \text{Im} \Sigma(E_{n\mathbf{k}}). \quad (2.49)$$

Here, $\tau_{n\mathbf{k}}$ is the scattering time and $E_{n\mathbf{k}}$ the quasiparticle energy.

For the description of satellite structures and to correctly represent spectral features of electron-boson interactions, however, the Fan-Migdal approximation has its limits. Firstly, the satellite energy are estimated by 50% compared to the experimental ones and secondly, the intensity of the plasmonic (polaron) satellite features is too high. [39] The framework of the cumulant expansion fixes these issues. It is an extension of the previously established formula for the spectral function originating from an alternative formulation of the single-particle Green's function. To the time-dependent non-interacting Green's function a so called cumulant factor $e^{C_{n\mathbf{k}}(t)}$ is introduced:[51]

$$G_n^0(\mathbf{k}, t) = ie^{i\varepsilon_{n\mathbf{k}}t + C_{n\mathbf{k}}(t)} \quad (2.50)$$

which proceeds into the spectral function:[52, 53]

$$A(\mathbf{k}, \omega) = \frac{1}{2\pi} \sum_n \text{Re} \int_{-\infty}^{+\infty} dt e^{i(\omega - \varepsilon_{n\mathbf{k}})t + C_{n\mathbf{k}}(t)} \quad (2.51)$$

The practical notation of the cumulant expansion suited for numerical simulations was reported by [7, 8, 54] and can be expressed as:

$$A(\mathbf{k}, \omega) = \sum_n [1 + A_{n\mathbf{k}}^{\text{S1}}(\omega) * + A_{n\mathbf{k}}^{\text{S1}}(\omega) * A_{n\mathbf{k}}^{\text{S1}}(\omega) * + \dots] A_{n\mathbf{k}}^{\text{QP}}(\omega). \quad (2.52)$$

Here $*$ is a convolution product and $A_{n\mathbf{k}}^{\text{QP}}(\omega)$ is the quasiparticle spectral function of Eq. 2.48 evaluated in the ‘‘on the energy shell’’ approximation, in which the frequency dependence of the self-energy $\Sigma_{n\mathbf{k}}(\omega)$ is replaced by the KS energy $\omega = \varepsilon_{n\mathbf{k}}$ [51, 55]. The satellite spectral function is further given by: [9]

$$A_{n\mathbf{k}}^{\text{S1}}(\omega) = -\frac{\beta_{n\mathbf{k}}(\omega) - \beta_{n\mathbf{k}}(\varepsilon_{n\mathbf{k}}) - (\omega - \varepsilon_{n\mathbf{k}})\beta'_{n\mathbf{k}}(\varepsilon_{n\mathbf{k}})}{(\omega - \varepsilon_{n\mathbf{k}})^2}, \quad (2.53)$$

with $\beta = \pi^{-1} \text{Im} \Sigma_{n\mathbf{k}}(\varepsilon_{n\mathbf{k}} - \omega)\Theta(\omega)$ and β' denoting its first derivative. The first term in Eq. 2.52 corresponds to the quasiparticle peak of the photoemission spectrum, while he series of the following terms accounts for the simultaneous excitation of any number of plasmons. But the intensity of the satellite peaks for the excitation of three plasmons is already quite low, which is due to the low probability of the scattering process. That is why in present *ab-initio* calculations Eq. 2.52 is truncated to the second order term. [52]

An example for the good agreement between experiment and theory is shown for the

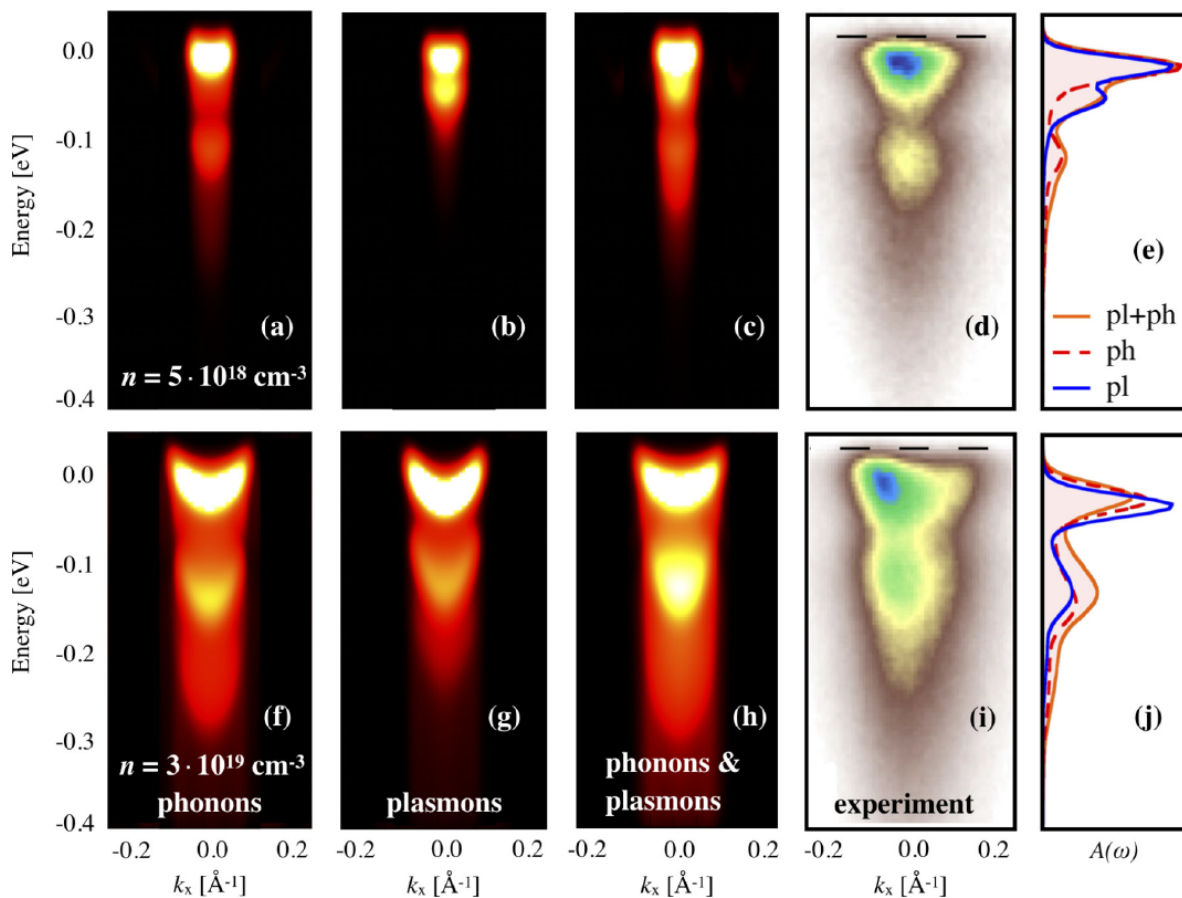


Figure 2.7.: Figures (a)-(e) show the theoretical (a)-(c) and experimental (d) ARPES spectra obtained for a doping level of $5 \times 10^{18} \text{ cm}^{-3}$ and (f)-(j) are for a free electron density of $3 \times 10^{19} \text{ cm}^{-3}$. (e) and (j) show the *ab-initio* spectral functions $A(w)$ in the cumulant expansion for these densities evaluated at the Γ high symmetry point due to the excitations of plasmons (pl), phonons (ph) and both of them together (pl-ph). The experimental ARPES spectra 2.7(d) and 2.7(i) were measured by Moser *et al.* [56]. [9]

polar material TiO_2 anatase in Fig. 2.7. Figures (a)-(e) show the theoretical (a)-(c) and experimental (d) ARPES spectra obtained for a doping level of $5 \times 10^{18} \text{ cm}^{-3}$ and (f)-(j) are for a free electron density of $3 \times 10^{19} \text{ cm}^{-3}$. Figs. 2.7(e) and 2.7(j) show the *ab-initio* spectral functions $A(w)$ in the cumulant expansion for these densities evaluated at the Γ high symmetry point (HP) due to the excitations of plasmons (pl), phonons (ph) and both of them together (pl-ph). The calculations nicely reproduce the experimental ARPES spectra 2.7(d) and 2.7(i) measured by Moser *et al.*[56]. In TiO_2 electron-phonon and electron-plasmon coupling is equally important to reach a complete picture of the scattering and excitation processes taking place. For HfS_2 both coupling effects will be taken into consideration and their importance will be explored.

3. Electron-boson interaction in hafnium disulfide

In this chapter, the results of this thesis are presented and can be roughly divided into three parts. In the first part (Sec. 3.1-3.4), the foundation is laid by the introduction of the material. Furthermore, experimental and computational conditions are described and preliminary analyses are performed. The second part (Sec. 3.5) is dedicated to the electronic and vibrational ground-state properties of HfS₂. For this purpose, the measured and calculated data were investigated and compared. That last part (Sec. 3.6 and 3.7) deals with many-body effects in the material brought forth by n-type doping. The examination of the spectral function leads to new insights and a simplistic model for the surface high-frequency dielectric function is proposed.

3.1. Transition-metal dichalcogenides

TMDs encompass a wide range of materials consisting of one transition metal atom M and two chalcogenide atoms X resulting in the chemical formula MX₂. They are layered van der Waals materials and thus part of the large class of so-called two-dimensional (2D) materials. The covalent bonding between the atoms is strong within a layer, while the van der Waals bonding between the layers is weak. The binding strength is also reflected in the lattice vectors, with typical values of 3 – 4 Å for *a* and 6 Å for *c*. In the formation of these layered structures the asymmetric coordination of the anions is balanced by the polarization energy, stressing the polarizability of the ions of such compounds [57]. The force constants of the Raman active intralayer vibrational modes (E_{2g}^2), of e.g. MoS₂, are much higher than the interlayer ones A_{1g} . The different vibrational modes are presented in Fig. 3.1(a). The anisotropy of these materials due to the van der Waals gap continues to their optical and transport properties and offers possibilities for further modification of their properties through intercalation. [58]

With regard to their band structure, TMDs appear in the form of metals, semimetals or semiconductors, but they can also exhibit more exotic states as topological insulators or superconductors [60]. Due to their orbital occupation group V compounds are metals with a partially filled d_{z^2} band, while group IV and VI tend to be semiconductors. The group IV materials exhibit band gaps in the order of 1-2 eV with filled *s*- and *p*-orbitals of the chalcogenide atoms and empty *d*-orbitals of the transition metal atoms. They usually occur in a 1T-structure, while the group VI materials exhibit 2H-structures. The d_{z^2} band of the later group is filled since they have two electrons “per formula unit” and thereby lower the band energy enough to overcome the Madelung energy. The difference between the 1T- and the 2H-structure is presented in Fig. 3.1(b). [61, 62]

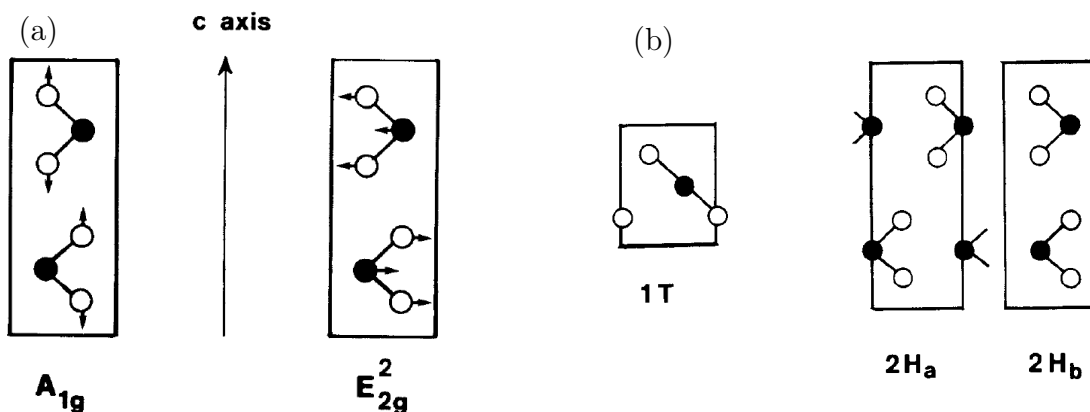


Figure 3.1.: (a) Interlayer A_{1g} and intralayer E_{2g}^2 vibrational modes of the MoS_2 . (b) Crystal structures found in transition-metal dichalcogenides (TMDs) with one layer per unit cell of trigonal symmetry cell (1T) and two layers per unit cell of hexagonal symmetry (2H). The filled and hollow spheres represent transition metal and chalcogenide atoms, respectively. [59]

In the context of miniaturization of transistors and other electrical components, reducing the TMDs to a single 2D monolayer is of great interest and reveal further promising physical properties of the materials. Since the interlayer bonding is weak the two dimensionality can be achieved by exfoliation of the layers. That way TMDs exhibit a broad variety of enhanced electronic properties, such as Mott transitions, the quantum spin Hall effect and superconductivity. [63–66]

A physical quantity key to understand this features is the dielectric response of the materials, which determines the electrostatic properties and the scattering processes due to electron-phonon and electron-plasmon coupling. These influence *inter alia* optical and transport properties. [67]

3.1.1. Crystal structure Hafnium disulfide

HfS_2 belongs to the class of TMDs and consists of one hafnium atom from the group 4 elements (transition-metal) and two sulfur atoms from the group 16 elements (chalcogens). It forms 1T-structured monolayers corresponding to a hexagonal Hf lattice sandwiched between two layers of hexagonally packed S atoms. In this arrangement, the Hf atom is octahedrally coordinated by the chalcogens, as shown schematically in Fig. 3.2 (a). The space group of 1T-structures is the $P\bar{3}m1$ and the lattice parameters of HfS_2 are $a = b = 3.64 \text{ \AA}$, $c = 5.84 \text{ \AA}$ with $\alpha = \beta = 90^\circ$, $\gamma = 120^\circ$ [68]. The hexagonal unit cell of HfS_2 leads to a hexagonal BZ with its characteristic high-symmetry points shown in Fig. 3.2 (b).

The monolayers are linked by van der Waals interactions and can be separated using different exfoliation methods. If not stated differently, the results presented in this thesis are obtained for bulk HfS_2 .

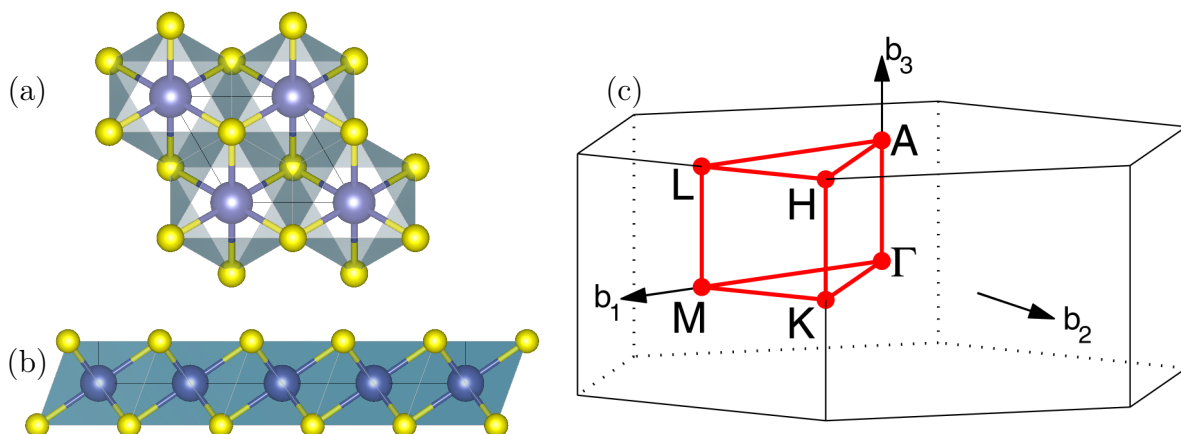


Figure 3.2.: (a) Top and (b) side view of the crystal structure of HfS₂ visualised with the VESTA (Visualization for Electronic and STructural Analysis) software package [69]. The blue colored atoms resemble hafnium and the yellow colored ones sulfur. (c) hexagonal BZ [cite: commonwiki].

3.2. Experimental conditions

The ARPES experiments were conducted by Sanjoy Mahatha from the Rosnagel group at German electron-synchrotron radiation source (DESY)/Kiel University. HfS₂ single crystals were grown by chemical vapor transport at the in-house facilities. The measurements were performed at beamline P04 of PETRA III at DESY using the ASPHERE photoelectron spectroscopy endstation. The sample temperature was 10 K. *In situ* doping of the HfS₂ samples was achieved by depositing potassium atoms from an alkali metal dispenser (SAES Getters) on the surface. The dopant atoms adsorbed on the surface but likely did not intercalate into the van der Waals gaps of the layered structure. The area probed by the synchrotron beam had a size of approximately $15\mu\text{m} \times 15\mu\text{m}$, the photon energies used and the corresponding energy resolution of the ARPES measurements were within a range of 260 eV- 450 eV and 50 meV- 80 meV, respectively. The Fermi map of the doped HfS₂ sample in Fig. 3.15 was more specifically collected at the photon energy of 432 eV.

3.3. Computational details

DFT calculations were performed based on the plane-wave pseudopotential method as implemented in Quantum ESPRESSO materials simulation suite version v.6.6 [70]. WANNIER90 [71] and the Electron-Phonon-Wannier (EPW) codes [72] were used for Wannier-function interpolation and electron-plasmon coupling simulations. The generalised gradient approximation to DFT of Perdew, Burke and Ernzerhof (PBE) for the exchange-correlation functional [29] and optimised norm-conserving Vanderbilt (ONCV) pseudopotentials [73] were used, with a plane wave kinetic energy cutoff of 120 Ry and a $12 \times 12 \times 6$ k -point mesh to sample the hexagonal BZ. The maximally localised Wannier functions were constructed starting from a $6 \times 6 \times 3$ \mathbf{q} -grid. The effect of n-type

doping was included in the virtual crystal approximation through a rigid shift of the Fermi energy. The first-principles spectral functions due to electron-plasmon interaction were obtained from the cumulant expansion method [52] using the electron-plasmon self-energy as implemented in EPW.

3.4. Preliminary analyses

To ensure the physicality of the first-principles calculations and the stability of the numerical results against changes of the computational parameters, preliminary analyses need to be made at the beginning of every calculation of a material. The following section focuses on establishing the optimal computational parameters for the subsequent investigation of the electronic properties of HfS₂. The aim of the analyses is the minimisation of the total energy, stress and forces of the compound to obtain the converged ground state of the system.

3.4.1. Convergence studies

The first parameter examined for convergence is the kinetic energy cutoff introduced in sec. 2.1.2. It corresponds to the number of \mathbf{G} -vectors used for expanding the Kohn-Sham orbitals and density in a basis. The computational cost of the calculations is determined by the energy cutoff and therefore this parameter requires careful consideration. Fig. 3.3(a) shows the dependence of the total energy on the kinetic energy cutoff and indicates a good convergence towards cutoffs higher than 100 Ry. An kinetic energy cutoff of 120 Ry was thus used for all further calculations.

Equally important is the choice of the k -point grid. It determines the number of points in the first BZ of the reciprocal space over which the integration is performed. The k -points should be evenly distributed to reliably map the entire BZ. This is accomplished in Quantum ESPRESSO by defining homogeneous grids in reciprocal space according to the Monkhorst-Pack algorithm [74]. In Fig. 3.3(b), the total energy was plotted against the number of k -points. The curve shows a well-behaved convergence trend. The difference in the total energy between the different number of k -points is smaller than $3 \cdot 10^{-6}\%$ when increasing the grid density from 726 to 1350 reducible k -points. For that reason, a $12 \times 12 \times 6$ k -point mesh was chosen for the calculation of the band structure, corresponding to 864 reducible (100 irreducible) k -points.

Finally, a structural relaxation was carried out to ensure that the computed crystal structure is dynamically stable, indicated by vanishing atomic forces and stress tensor. The first-principles atomic positions and the crystal-lattice vectors spanning the unit cell are given in Table 3.1. The unit cell volume associated with these vectors is $V_{\text{uc}} = 457.5 \text{ \AA}^3$. A summary of all computational parameters is given in in Table 3.2.

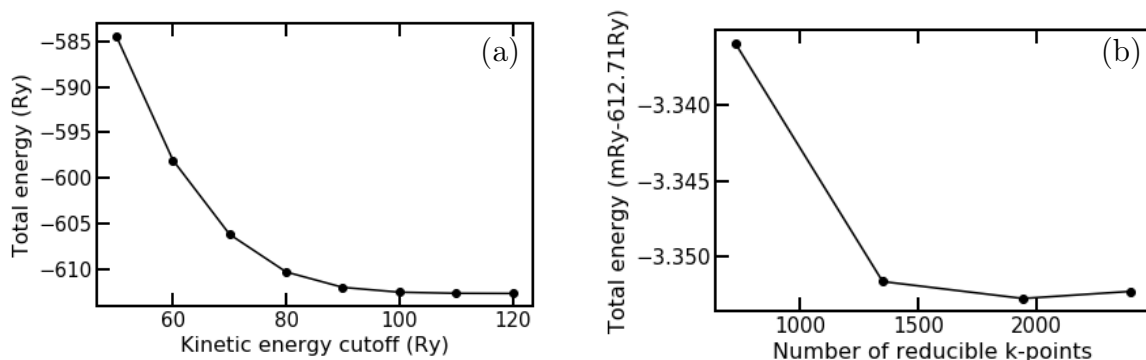


Figure 3.3.: Total energy of HfS_2 as a function of the cut-off energy (a) and the number of k-points (b). The energy axis of the plot (b) is offset by 612.71 Ry due to the minimal change in the total energy.

Atomic positions (crystal)				Lattice vectors (angstrom)	
Hf	0.00	0.00	0.00	DFT	Experiment [68]
S	$0.\bar{6}$	$0.\bar{3}$	0.76	a = 3.63	a = 3.64
S	$0.\bar{3}$	$0.\bar{6}$	0.24	c = 5.95	c = 5.84

Table 3.1.: *Ab-initio* crystal structure parameters of HfS_2 . The atomic positions are given in units of the crystal lattice vectors.

3.5. Electronic and vibrational properties

The band structure of HfS_2 evaluated along the MK Γ MLHAL-high-symmetry-path is shown in Fig. 3.4 (a). The in-plane path was chosen to match the measurements and allow a comparison of the MK Γ M- and the LHAL-planes of the 3D BZ. In good agreement with literature values from theory and experiment, the direct fundamental gap at Γ is around 1.9 eV and the indirect bandgap between Γ and the CBM at L is around 1.1 eV. [75–77] In Fig. 3.4 (b) the ARPES measurements along the MK Γ M-high-symmetry-path are shown as an intensity plot ranging from dark brown (maximum intensity) to white (minimum intensity). The first-principles calculations colored in blue agree quite well with them. A small deviation occurs at the K-point: In the measurements the highest valance band appears to dip towards the lower bands, in contrast to the calculated one. This deviation might be attributed to surface effects in the measurements.

E_{cut}	120 Ry
reducible k -point mesh	$12 \times 12 \times 6$
Pseudo potential	ONCV pseudopotentials [73]
XC-functional	PBE [29]

Table 3.2.: Summary of computational parameters employed in the *ab-initio* calculation of the HfS_2 band structure.

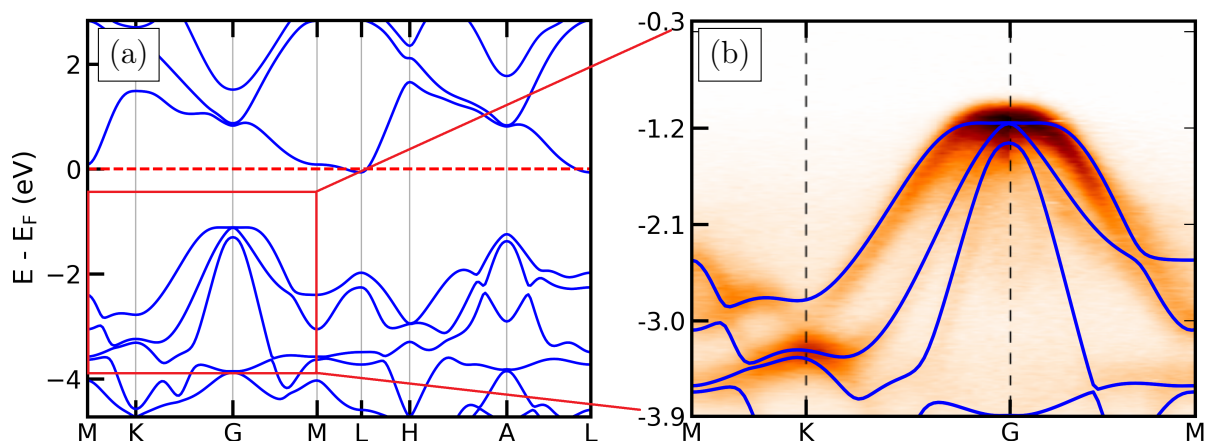


Figure 3.4.: (a) first-principles electronic band structure of HfS_2 . (b) Comparison with angle-resolved photoemission spectroscopy ARPES measurements. The red dashed line in the plot (a) marks the Fermi energy of the doped compound.

Dimensionality and bandgap

The following calculations have been performed to study the effect of dimensionality on the layered van der Waals material HfS_2 and the dependence of the electronic band structure on the interlayer distance is examined, since the interlayer distance between the monolayer is overestimated by 0.11 \AA as compared to the experimental measurements [68]. Furthermore, the dimensionality influences the position at which the n-dopants contribute their electrons to the conduction band of the doped HfS_2 . The CBM of the 2D HfS_2 is located in the L-M plane because its BZ is a projection of the three-dimensional (3D) BZ. In that case, the high-symmetry points L and M coincide, while the CBM of the 3D compound is at the L point. The interlayer distance is defined by the value of the lattice vector c , which specifies the distance between the Hf monolayers. In Fig. 3.5(a) the energy difference of the lowest conduction band at the high-symmetry points L and M is visualised as a function of the interlayer distance. In the equilibrium position with an interlayer distance of around 6 \AA the energy difference between the two points is greatest and amounts to 152 meV . For larger c lattice vectors the difference decreases because the interaction between the layers becomes weaker and approaches the 2D limit, in which L and M coincide. For interlayer distances smaller than 6 \AA the entire band structure is distorted owing to the overestimation of the interlayer coupling, resulting in a band-gap collapse and metal-like bands for an interlayer distance smaller than 4.5 \AA . The compression is equivalent to a strain along the z-axes of the material. Fig. 3.5(a) illustrates this behaviour and displays the indirect band gap between the valence band maximum (VBM) and the CBM located at the high-symmetry points Γ and L. The indirect band gap rapidly diminishes for interlayer distances smaller than 6 \AA . The band gap of the 2D limit is slightly larger and compares well with experimental values around 1.2 eV [15]. The band gap increase can be related to charge confinement within the material.

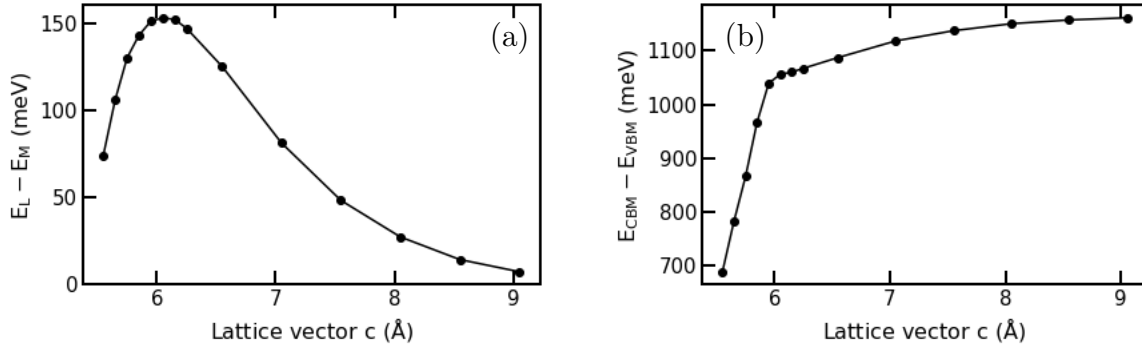


Figure 3.5.: (a) Energy difference between the high-symmetry points L and M of the lowest conduction band as a function of the interlayer distance of HfS₂. (b) Energy of the indirect band gap as a function of the interlayer distance of HfS₂.

3.5.1. Spin-orbit coupling

SOC is a relativistic effect describing the interaction of the spin of electrons with their orbital motions. As heavy elements with unfilled 5*d* orbitals such as Hf tend to exhibit strong spin-orbit coupling and increased hybridization, it is important to consider this interaction in the calculation. [78]

In Fig. 3.6 the band structure of HfS₂ with (black, continuous) and without (red, dashed) SOC is depicted, emphasising its importance and effect on the band structure. SOC leads to an avoidance of band crossings in the valance as well as the conduction bands and lifts the degeneracy of upper valance bands at the Γ point. This findings are in good agreement with literature calculations based on the same level of theory [16]. The VBM rises slightly in energy, while the CBM is lowered causing a small energy renormalization of the band gap in the meV range. The largest band splitting occurs at the Γ point between the second and third highest valance band is about 182 meV. The most interesting effect is the shift of the VBM to the Γ point leading to a flat band dispersion. The flat bands coincide with "massless" properties of particles populating these bands. This linear dispersion provides a good basis for the study of excitations and p-type (hole) doping could lead to emergent electronic applications.

3.5.2. Effective mass calculation

To treat the interaction of the electrons at the CBM properly, their effective mass at that point needs to be determined. Applying a parabolic band model to the dispersion, the effective mass can be determined using the following equation given in SI-units:

$$E_n(\mathbf{k}) = E_{n,0} + \frac{\hbar^2 \mathbf{k}^2}{2m^*} \quad \Rightarrow \quad m^* = \hbar^2 \left(\frac{d^2 E(\mathbf{k})}{d\mathbf{k}^2} \right)^{-1} \quad (3.1)$$

Here $E_n(\mathbf{k})$ is the energy of the band n at the momentum vector \mathbf{k} , \hbar is Planck's constant reduced by 2π and m^* is the effective mass. A second order polynomial fit of the form $(ax^2 + bx + c)$ in the vicinity of the CBM is performed including 5 \mathbf{k} -points

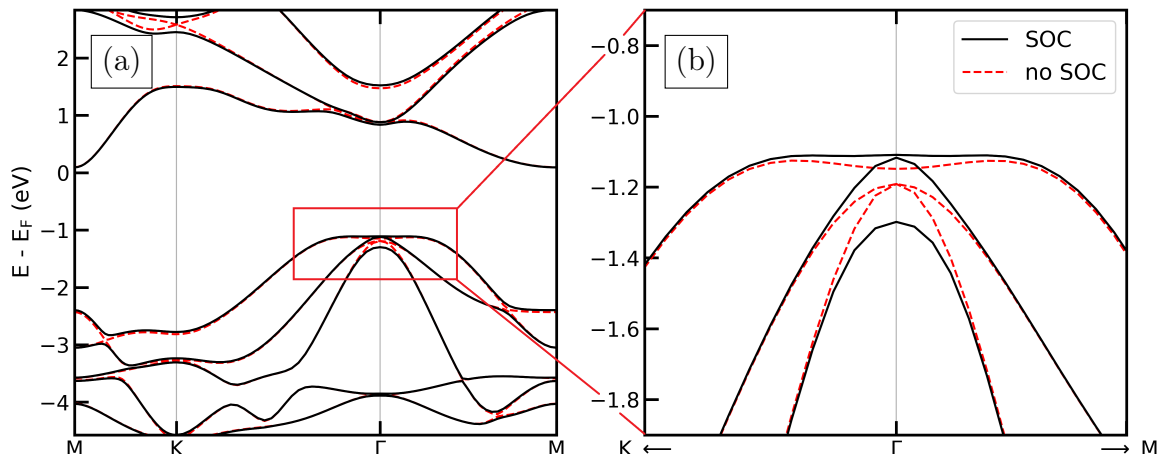
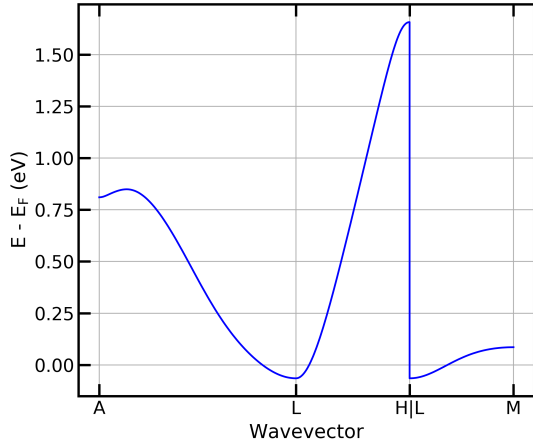


Figure 3.6.: Effect of spin-orbit coupling (SOC) on the electronic band structure of HfS_2 . The black (red dashed) line represent the band structure with (without) SOC beginning accounted for in the calculation.

towards each direction of the other high-symmetry points M, A and H. The effective mass of the electrons is thus obtained from a. This parabolic band model is a reasonable local approximation due to the parabolic dispersion relation of electrons in the vicinity of the band edges. Because of the anisotropy of the band dispersion towards the other high-symmetry points (M-L, A-L, L-H) in the BZ, the effective mass needs to be calculated along each path individually and averaged afterwards. To consider the total carrier density the following equation is used for the calculation:[79]

$$m_{\text{DOS}}^* = \sqrt[3]{g^2 m_1 m_2 m_3} \quad (3.2)$$

The abbreviation DOS stands for density of states, the indices 1,2,3 indicate the different directions in the BZ and g is a degeneracy factor. The important high-symmetry points for the considered band are visualised in Fig. 3.7 and the masses obtained by the parabolic fits are given in table 3.3 and compare well with literature values [80]. The resulting average effective mass is $m_{\text{DOS}}^* = 1.44 \cdot m_e$.



Path	$m_i^* [m_e]$
A-L	0.25
L-H	1.65
L-M	0.20

Table 3.3.: Effective masses of the electrons at the conduction band minimum along different high symmetry paths of the first Brillouin zone.

Figure 3.7.: Conduction band minimum of HfS_2 along the different high symmetry paths of the first Brillouin zone.

3.5.3. Iso-energy cuts and Wannier interpolation

In Fig. 3.8 iso-energy cuts -1.3 eV and -2.2 eV below the Fermi energy are illustrated for the crystal momenta spanning the k_x - k_y -plane. The measured intensity map ranges from dark brown (maximum intensity) to white (minimum intensity). The black dots are calculated k -points that match the energy of the experiment. The values for one unit cell were computed, while the remaining points were obtained by shifting that unit cell using the translation invariance. The blue lines in panel (a) mark the boundaries of the BZ with the Γ point centred in the middle, the M point in the middle of the face sides and the K point at the intersection of the face sides. Both *ab-initio* calculations match the experimental data very well within the first BZ. The neighbouring cells show minor deviations, which we attribute to a grid distortion of the experimental images originating from the geometry of the hemispherical analyser. To minimize this effect the first BZ was centred in the middle of the detector screen.

The k -point-grids required to enable these calculations are very dense. To minimize these computational costs, the data in Fig. 3.8 have been obtained via Wannier function interpolation. The Wannier function interpolation is a Fourier transform of the wave functions from reciprocal space to real space under the condition of maximal locality of the wave function orbitals in real space and a reverse transformation onto a denser grid.[71] The denser grid is also important to precisely determine the Fermi energy correctly calculate the electron-plasmon coupling matrix elements.

To make sure that the interpolation was successful, the interpolated band structure is plotted with the original one from the previous calculation. The agreement between them is verified in Fig. 3.9. The black lines are the first-principles electronic band structure of HfS_2 calculated with Quantum ESPRESSO, while the red dashed lines are the electronic band structure interpolation of WANNIER90. They are equivalent to each other.

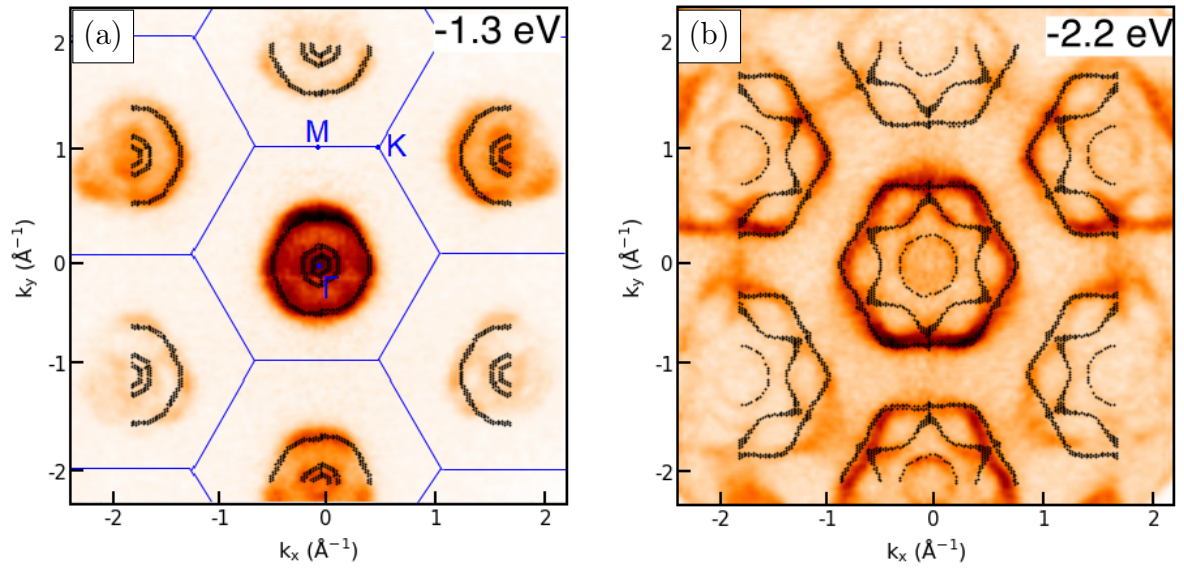


Figure 3.8.: Iso-energy cut of the k_x - k_y -plane -1.3 eV (a) and -2.2 eV (b) below the Fermi energy. The blue hexagons in (a) mark the area of the Brillouin zone with the Γ point centered in the middle, the M point in the middle of face sides and the K point at the intersection of the face sides. The calculated k-points are plotted in black.[Edit: try white color for Gamma]

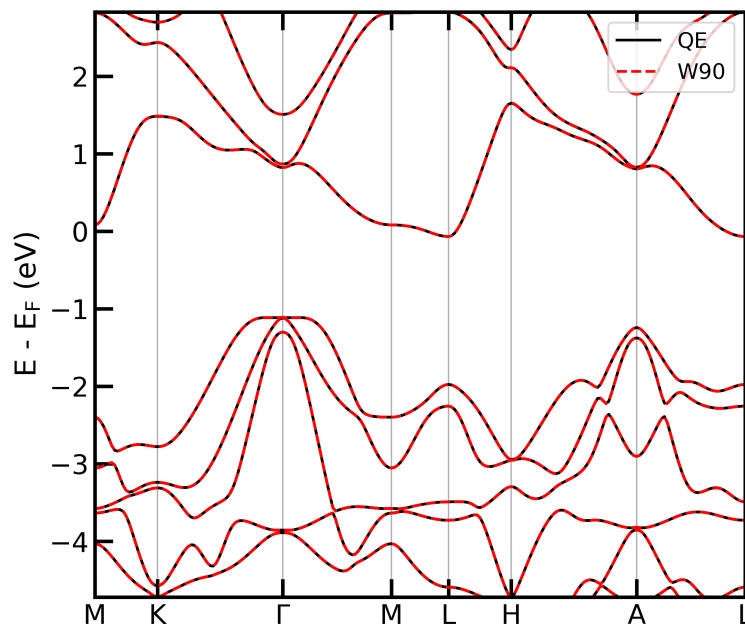


Figure 3.9.: Electronic band structure of HfS_2 calculated with Quantum ESPRESSO (black solid lines) and interpolated electronic band structure from WANNIER90 (red dashed lines).

3.5.4. Phonon dispersion

The phonon dispersion of HfS_2 obtained from density functional perturbation theory is shown in Fig. 3.10 and is consistent with literature calculations [81, 82]. The unit cell of the crystal consists of three atoms, resulting in a total of nine phonon modes with three acoustic and six optical modes, respectively. Four of the optical modes are transverse (TO), while the remaining two are longitudinal (LO). The second and third highest energy phonon modes appear to jump at Γ point. At that point the path between the high symmetry points is changed from the in-plane ($k_x - k_y$ -direction) towards to out-of-plane (k_z -direction) direction. The effect causing this jump is the LO-TO-splitting present in polar materials. It leads to the removal of degeneracy between the longitudinal optical (LO) and transverse optical (TO) phonons at the BZ centre ($k=0$). The polarisation in such materials is related to the crystal symmetry and thereby affects the phonon dispersion. The highest phonon mode has a frequency of around 43 meV.

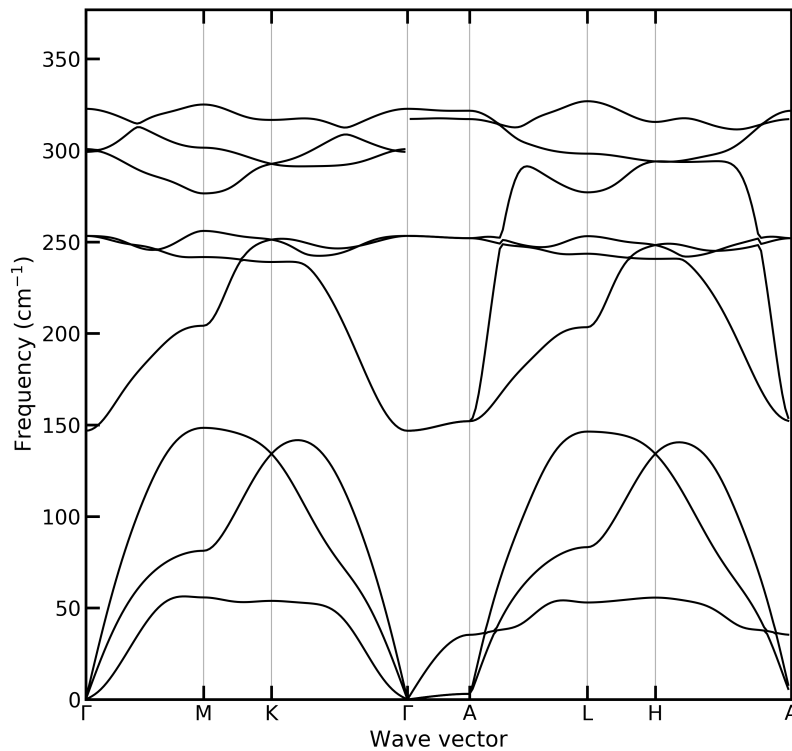


Figure 3.10.: Phonon dispersion relation of HfS_2 obtained from density functional perturbation theory.

3.6. Doping and electron-plasmon interaction

While the physical properties of pristine group-IV TMDs, like HfS_2 , are well studied [75, 81, 82], their doped counterparts are rather unexplored. However, the doping of semiconductors in general brings forth a bright spectrum of many-body phenomena to be studied by spectroscopic methods and should thereby be used as a tool to reach a deeper physical understanding of the processes occurring also in intrinsic semiconductors. The focus of the chapter is on the electron-plasmon interaction, as it is assumed to be the dominant interaction influencing the properties of the spectral function.

3.6.1. Doping concentration and Fermi energy

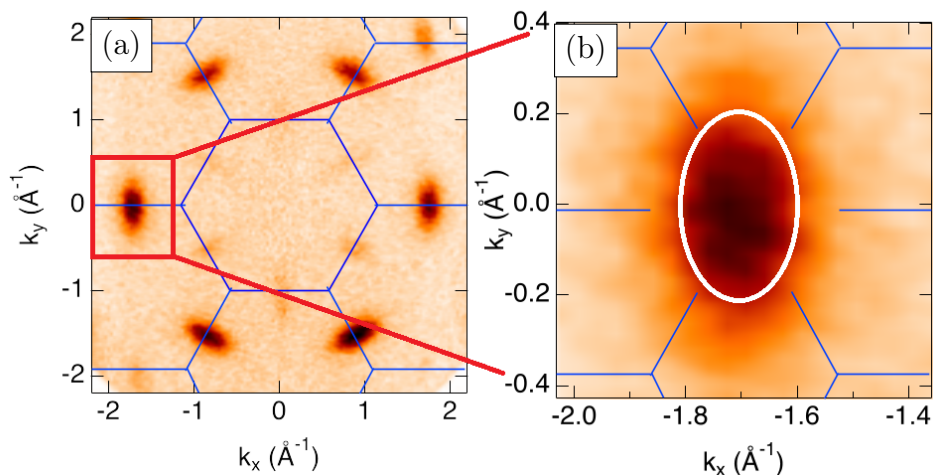


Figure 3.11.: Iso-energy measurement of the k_x - k_y -plane near the Fermi energy. The blue hexagons mark the area of the Brillouin zone. The white ellipse in (b) is used to estimate the size of one Fermi pocket.

In Fig. 3.11(a) the iso-energy measurement in the k_x - k_y -plane of the CBMs is presented and illustrates some salient features. Firstly, the electron pockets of the first BZ are quite weak compared with the ones outside of it. This is due to electron selection rules of the dipole-transition matrix elements. They allow transition with a certain probability and thereby intensify or attenuate spectral features in the photocurrent of the ARPES signal. The initial estimate of the doping concentration was calculated by inspection of the electron pockets at the CBM in Fig. 3.11(b) and corresponds to the Fermi surface of the doped material, since the Fermi energy is located in the lowest conduction band. The area of the electron pocket in Fig. 3.11(b) is framed by a white ellipse, of which the major and minor axis radii are $a = 0.2 \text{\AA}^{-1}$ and $b = 0.1 \text{\AA}^{-1}$, respectively. There are six electron pockets and each pocket contributes half of the ellipse to a BZ. Therefore, the number of electrons N_{el} per unit cell can be estimated by the formula:[83] (details see

Appendix Fig. A.1)

$$N_{\text{el}} = \frac{3ab}{2\pi} \times 10^{16} \text{cm}^2 = 0.01 \quad (3.3)$$

The number of electrons per unit cell is directly linked to the free electron density by unit cell volume V_{uc} :

$$n = \frac{N_{\text{el}}}{V_{\text{uc}}}, \quad (3.4)$$

The calculated 3D unit cell volume of HfS_2 is $V_{\text{uc}} = 457.5 \text{ a.u.}^3$. Therefore the free electron density of the material is $n = 2.2 \cdot 10^{-5} \text{ a.u.}^{-3} = 1.5 \cdot 10^{20} \text{ cm}^{-3}$.

With this information as a basis, the doped system can be treated in *ab-initio* calculations, by considering an excess number of electrons per unit cell volume with a compensating homogeneous, positive background. Because the additional number of electrons per unit cell is so small, a supercell treatment including actual dopant atoms is numerically too expensive. Furthermore, in a supercell treatment the band structure would be folded back into the BZ multiple times because of the connection between real space and reciprocal space. To determine the Fermi energy precisely an EPW calculation on a dense k -grid of $150 \times 150 \times 60$ was performed. The Fermi energy was calculated for multiple electron densities, which are listed in Table A.1 in the appendix. In the first column the Fermi energy of the zero free electron density is chosen to coincide with the CBM. In Fig. 3.12(a) the Fermi energy is plotted as a function of the additional number of electrons per unit cell. The graph shows a square root behaviour corroborating the parabolic band model used for the effective mass calculations and the HEG. The Fermi energy corresponding to the free electron density of $n = 1.5 \cdot 10^{20} \text{ cm}^{-3}$ is $E_{\text{F}} = 9.735 \text{ eV}$.

In Fig. 3.12(b) the plasmon frequency is plotted as a function of the additional number of electrons per unit cell. In comparison to Eq. 2.36 the formula for the frequency is refers to the unit cell and the electron mass is replaced by the effective mass to meet the dispersion of the CBM and is given in SI-units:

$$\omega_{\text{pl}} = \sqrt{\frac{4\pi N_{\text{el}} e^2}{V_{\text{uc}} m^* \epsilon_{\infty}}}. \quad (3.5)$$

Here ϵ_{∞} is the high-frequency dielectric constant. It describes the behaviour of the medium in the limit of high frequencies at which the nuclei are too slow to react to perturbations, hence on that time scale phonons can't be excited.

3.6.2. Electron-plasmon coupling

In Fig. 3.13 the calculated real and imaginary part of the electron self-energy Σ due to electron-plasmon interaction at a doping concentration of $n = 1.5 \cdot 10^{20} \text{ cm}^{-3}$ is illustrated. The imaginary part of the self-energy is close zero for values smaller than -0.4 eV and exhibits a characteristic peak at the pole of the real part ($\text{Re } \Sigma = 0$) around the energy $\epsilon_{\mathbf{k}} - \hbar\omega_{\text{pl}}$. This feature originates from the plasmon peak in the dielectric function

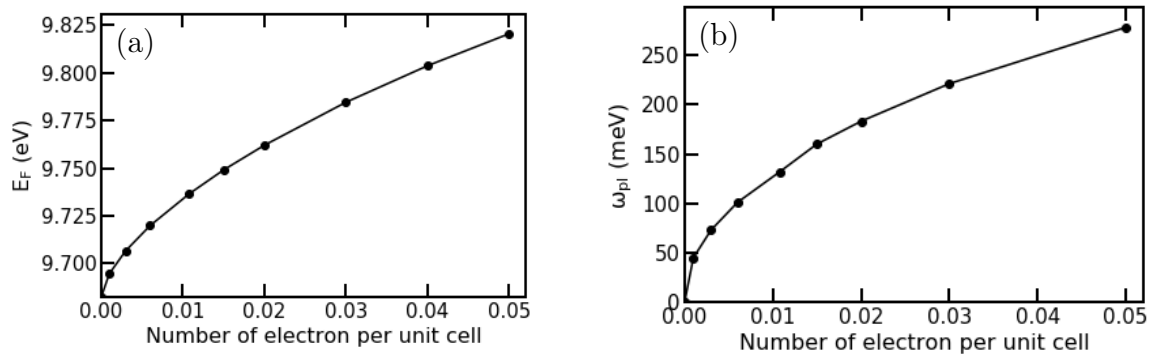


Figure 3.12.: Dependence of the Fermi energy (a) and plasmon frequency (b) on the free electron density.

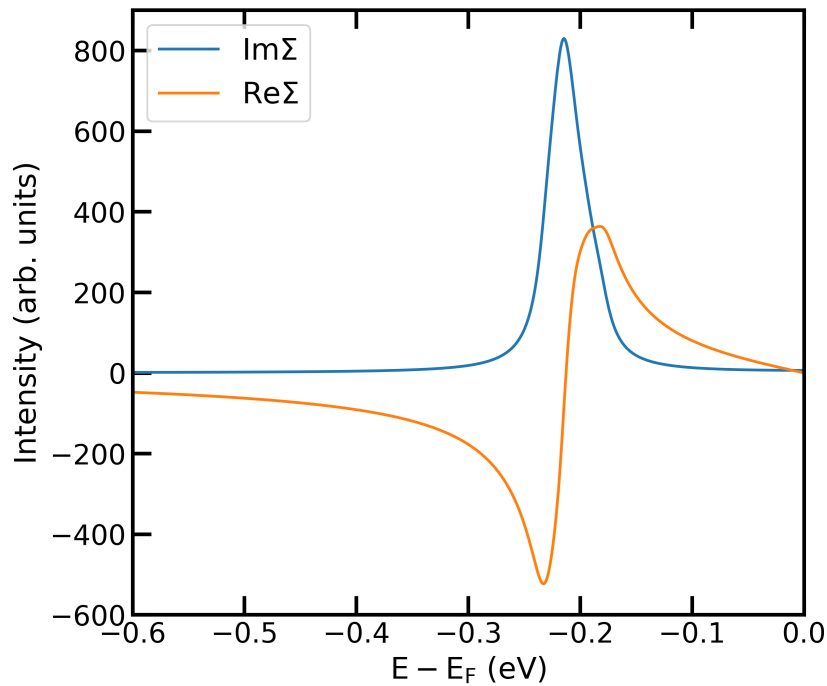


Figure 3.13.: Real (Re) and imaginary (Im) part of the electron self-energy Σ due to electron-plasmon interaction for HfS_2 at a doping concentration of $n = 1.5 \cdot 10^{20} \text{ cm}^{-3}$. Gaussian smearing 10 meV

within the GW framework and the RPA. The poles in the real part yield the feasible energy spectrum for the collective density fluctuations. The curves of both parts show smooth behaviour and their interdependency is clearly visible.

When calculating the self-energy there is a strong dependence between the \mathbf{k} -point sampling and the \mathbf{k} -point broadening introduced by a Gaussian smearing parameter η occurring in equation 2.39. To compute coupling effects correctly, the broadening applied to the \mathbf{k} -points must be large enough to ensure an overlap of the points. The smooth functions were achieved by a \mathbf{k} -point grid of $60 \times 60 \times 30$ and a gaussian smearing of 10 meV.

The effect of the broadening on the spectral function of the CBM in the Fan-Midgal approximation for the free electron density $1.5 \cdot 10^{20} \text{ cm}^{-3}$ and a high-frequency constant of 7.6 is demonstrated in Fig. 3.14. The plasmonic polaron satellite is located at the pole of the electron self-energy. For the smallest Gaussian smearing of $\eta = 20 \text{ meV}$ the quasiparticle peak and the plasmonic polaron satellite are sharp and clearly separated from each other. The larger the broadening becomes the stronger these features are smudged, leading to a broad and lower quasiparticle peak with a long tail but no clear satellite visible. In this calculation step, before the post-processing and accounting for the experimental resolution, it was important to use a small smearing to calculate the coupling strength correctly and make out the satellite features as clear as possible.

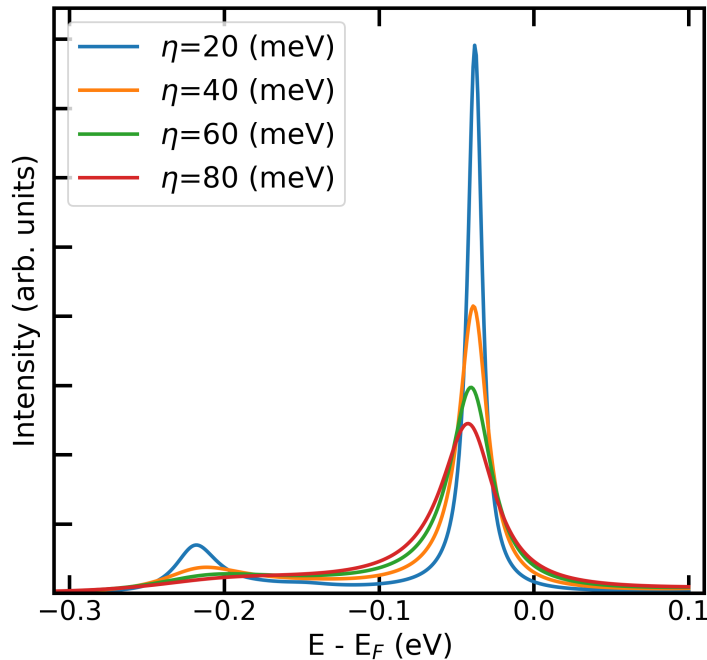


Figure 3.14.: Spectral function $A(\omega)$ in the Midgal-approximation for the conduction band minimum for an density of $1.5 \cdot 10^{20} \text{ cm}^{-3}$ and a high-frequency constant of 7.6. The intensity of $A(\omega)$ for different electron smearings η is plotted as a function of the energy relative to the Fermi energy.

3.7. Spectral features

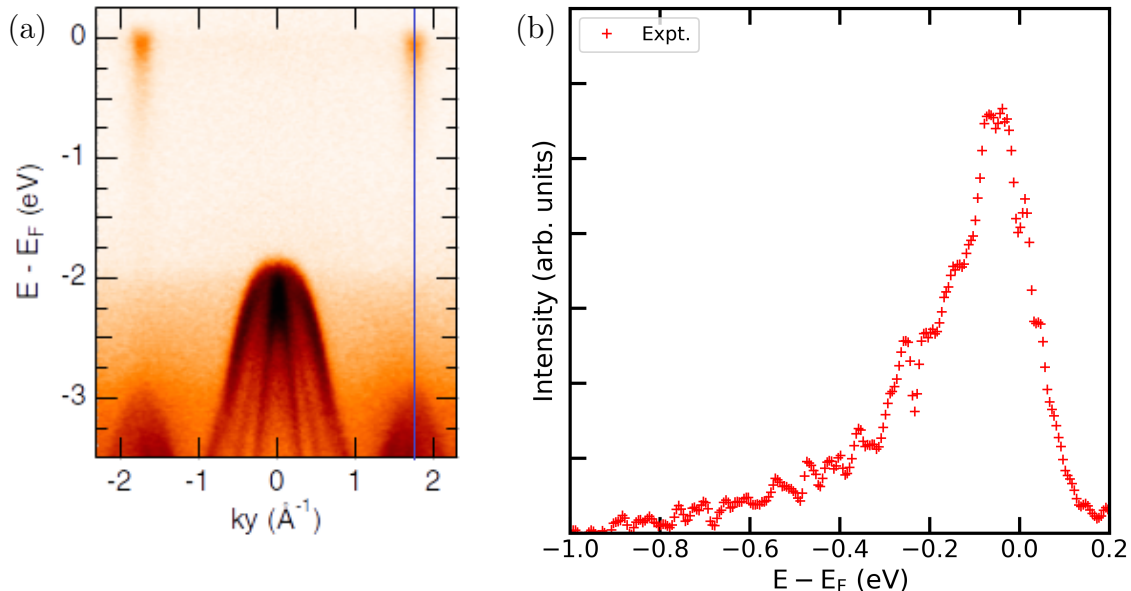


Figure 3.15.: ARPES measurements of the doped HfS_2 sample. (a) Band structure showing the Γ point at $k_y = 0 \text{ \AA}^{-1}$ and the CBM around $|k_y| = 1.8 \text{ \AA}^{-1}$. (b) Spectral function of the right CBM taken at the blue line.

The band structure of the doped material obtained by ARPES measurements is given in Fig. 3.15(a). The intensity of the measurement is reflected in the colour of the plot, ranging from dark brown (highest intensity) to white (minimum intensity). The Fermi pockets of the CBM are located around $|k_y| = 1.8 \text{ \AA}^{-1}$. The intrinsic spectral function $\tilde{A}(\omega')$ of the CBM was extracted at the blue line. To reduce the noise in the spectral function the measured photocurrent of two k -points at the immediate vicinity of the CBM with a distance of $\Delta k = 0.03 \text{ \AA}^{-1}$ were added up allowing a more qualitative analysis of the data.

The Shirley background accounting for the secondary electrons was calculated with Eq. 2.3.1 by integrating $\tilde{A}(\omega')$ up to the chemical potential μ . The subtraction of the background is shown in the appendix Fig A.2. The resulting spectral function $A(\omega)$ shown in Fig. 3.15(b) is characterized by a broad quasiparticle peak exhibiting a shoulder around 200 meV away from the quasiparticle peak, ending in a long tail towards lower energies of up to -1 eV. Within the shoulder of the spectral function a dip occurs that could indicate the separation of the quasiparticle peak and the satellite peak. Since the highest energy of a phonon mode is around 43 meV such expanded features can not be attributed to electron-phonon interaction. Furthermore, for such high levels of electron doping ($n \sim 10^{20} \text{ cm}^{-3}$), materials typically enter a Fermi liquid regime in which the electron-plasmon coupling also exceeds the electron-phonon coupling in strength [4, 52].

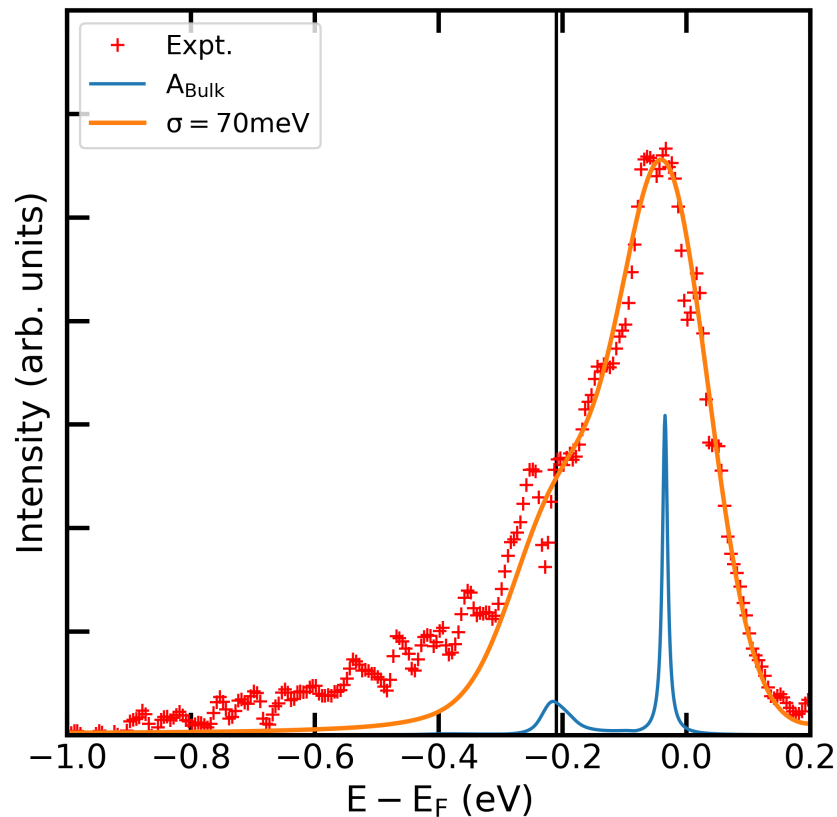


Figure 3.16.: Experimental data obtained from ARPES measurements (red crosses), calculated spectral function within the cumulant expansion (blue line) and convoluted spectral function performed with a Gaussian distribution (yellow line). The standard deviation for the Gaussian convolution is $\sigma = 70$ meV. The vertical black line is introduced at the satellite peak for visual guidance. The high frequency dielectric constant of 6.2 used for the calculation represents the bulk.

In Fig. 3.16 the spectral function of the CBM computed for the bulk material is plotted in blue. To account for the experimental resolution of 50-80 meV, impurities and other broadening factors a convolution with a Gaussian function was performed (yellow line). (Its width) the standard deviation of $\sigma = 70$ meV for the Gaussian distribution was chosen to match the right-hand slope of the measurements and lies in the range of experimental resolution. The intensity of the convoluted spectral function was adjusted to the height of the quasiparticle peak. Since the intensity of the measured photocurrent is given by the number of electrons per area of the detector screen, the absolute intensity of the measurement is also relative, which justifies the alignment of the peaks. The Fermi energy of the doped HfS₂ was computed accurately on a fine grid and was chosen to be the reference point of the calculated as well as the experimental data. The high-frequency dielectric constant used in Fig. 3.16 corresponds to the bulk volume value reported by

Lucovsky et. al and others [84, 85]. The spectral function computed with that value exhibits a small shoulder around 0.2 eV below the Fermi energy where the satellite peak is located. For visual guidance a vertical black line was positioned at the top of the satellite peak. The line highlights that the satellite peak of the bulk spectral function is located before the dip in the measured spectral function. The shoulder that occur in the calculated spectral function supports the assumption that electron-plasmon interaction plays a dominant role in the emergence of these features, but the calculated coupling is weaker than the measurements suggest. To exhibit a more pronounced shoulder in the spectral function the strength of the coupling should be stronger. At the interface between sample and vacuum such a stronger coupling is present. It is rooted in the a lower high-frequency dielectric constant obtained by the following model:

$$\varepsilon_S = 1 + \frac{\chi_{\text{bulk}} + \chi_{\text{vac}}}{2} = 1 + \frac{\varepsilon_\infty - 1}{2} = \frac{\varepsilon_\infty + 1}{2}, \quad (3.6)$$

where χ_{bulk} and χ_{vac} are the electric susceptibility of the bulk and the vacuum. As bulk and vacuum make up have of the space of the interface both susceptibilities contribute equally to the high-frequency dielectric constant. In this model, the assumption is made that the dominant plasmons involved in the interaction are located at the surface of the Van-der-Waals material, i.e. the electrons contributed by the n-dopants are present on the surface of the sample. Since the doping was achieved by depositing the potassium atoms on the surface of the samples by a dispenser, the atoms probably did not penetrate into deeper layers. Therefore, it can be assumed that the increase of the free electron density is also localised near the surface, physically supporting this simplistic model.

In Fig. 3.17 the interface spectral function computed with a high-frequency dielectric constant of 3.6 is plotted in blue. The effect of the change of the high-frequency dielectric constant is immense. The coupling is intensified and the plasmon frequency rises to a value of $\omega_{\text{pl}} = 210$ meV. The ratio of the peaks is renormalised leading to the emergence of a pronounced shoulder in the spectral function. To make qualitative comparisons with Fig. 3.16 the same multiplication factor for the intensity of the calculated spectral function was used. Compared to the bulk spectral function the satellite peak of the interface spectral function is shifted towards lower energies and is thereby located behind the dip in the shoulder of the experimental spectral function, which is illustrated by the black line. Tough the intensity of the satellite peak is even a bit too high, due to an overestimation of the electron-plasmon coupling, the distance between the peaks determined by the plasmon frequency ω_{pl} matches quite well. In Fig. A.3 of the Appendix the calculated spectral function within the cumulant expansion formalism is presented again with a higher multiplication factor for the intensity, emphasising the alignment of the ARPES measurement and the *ab-initio* calculation using QuantumEspresso and EPW. The interface model presented in the thesis supports the idea that surface effects have an influence on the measured spectral function.

The extension of the calculated shoulder ends around -0.5 eV, but the long tail of the measurements up to -1.0 eV could not be reproduced. The tail is due to higher order effects and inelastic scattering events that are not account for in the simulation. Because it (the tail) exhibits no clear characteristics, a more precise description of the processes

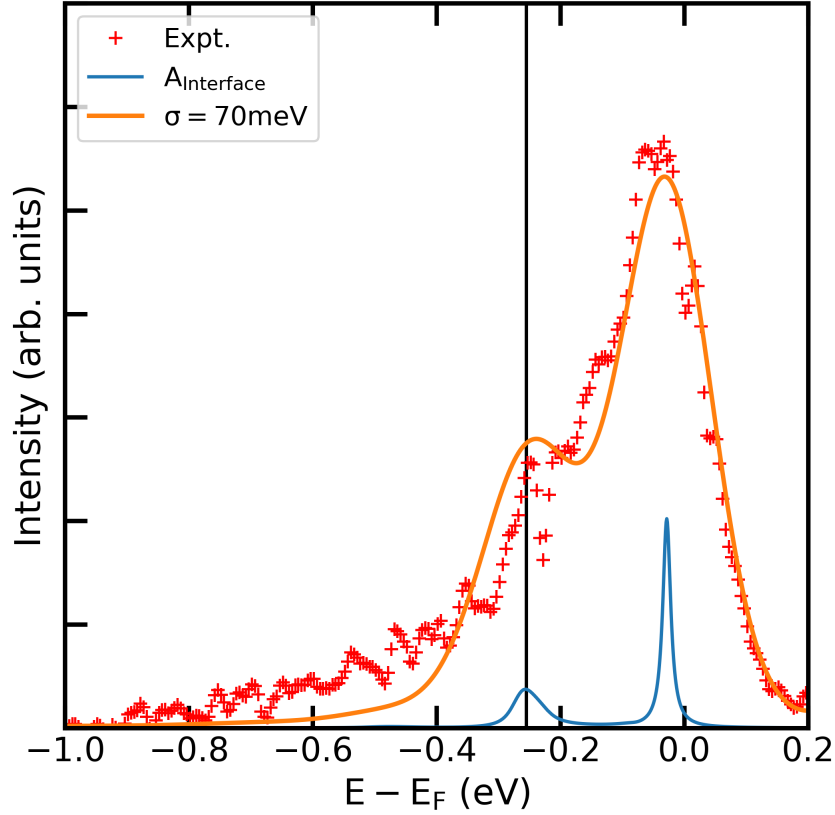


Figure 3.17.: Experimental data obtained from ARPES measurements (red crosses), calculated spectral function within the cumulant expansion (blue line) and convoluted spectral function performed with a Gaussian distribution (yellow line). The standard deviation for the Gaussian convolution is $\sigma = 70\text{meV}$. The vertical black line is introduced at the satellite peak for visual guidance. The high frequency dielectric constant of 3.6 used for the calculation represents the interface of the material.

that lead to its appearance is difficult. Nevertheless, the level of agreement reached between theory and experiment is quite remarkable. It underpins that the origin of the spectral function features are of plasmonic nature and that surface effects further influence the spectral function features.

The results demonstrate that enhanced electron-plasmon coupling occurs in heavily doped HfS_2 and encourages to search for electron plasmon coupling in other TMDs. The coupling leads to satellite peaks in the spectral function, which lie in the range of hundreds of meV and are determined by the plasma frequency of the density of free electrons in the conduction band. Significantly, we demonstrated that the correlation between electrons and plasmon is increased near the surface and may be amenable to tuning by applying suitable doping methods.

4. Conclusions and Outlook

In this thesis, a first-principles approach describing plasmonic polaron satellite structures in the spectral function of angle-resolved photoemission spectroscopy (ARPES) measurements was presented and applied to the transition-metal dichalcogenide (TMD) HfS₂. A simplistic model for the interface dielectric function was developed by comparing the measured and calculated data to account for surface effects. It was found that the satellite structures in the spectral function of the doped HfS₂ originate from electron-plasmon coupling and intensifies at the interface of the material.

First, the ground state properties of pristine HfS₂ were calculated using density-functional theory based on the plane-wave pseudopotential method as implemented in Quantum ESPRESSO. The calculated electronic band structure obtained in this framework matches the ARPES measurements quite well. The iso-energy cuts obtained by Wannier function interpolation further verify the agreement between theory and experiment. It was confirmed that HfS₂ exhibits strong spin-orbit coupling leading to a shift of the valence band maximum to the Γ point, resulting in a flat band dispersion. The largest band splitting occurs at the Γ point between the second and third highest valence band is about 182 meV. The dimensionality effect was investigated and evaluated in the two-dimensional limit. Bulk HfS₂ exhibits a slightly smaller indirect band gap of 1.1 eV compared to its 2D counterpart due to charge confinement within the material. Using a parabolic band model, the effective mass of the electrons at the conduction band minimum was determined to be $m_{\text{DOS}}^* = 1.44 \cdot m_e$. The phonon dispersion was calculated using density-functional perturbation theory and is consistent with literature calculations. LO-TO-splitting characteristic for polar materials was observed and the highest phonon mode with an energy of 43 meV elaborate. The boson energies for the electron-phonon coupling were insufficient to explain the broad satellite features of the spectral function measured by ARPES.

The focus was then put on electron-plasmon coupling present in the doped semiconductor. The free electron density of the highly doped HfS₂ sample was determined by the inspection of the Fermi pocket of ARPES iso-energy measurements. The corresponding Fermi energy to the free electron density of $n = 1.5 \cdot 10^{20} \text{ cm}^{-3}$ is $E_F = 9.735 \text{ eV}$ and was computed on a dense k -grid of $150 \times 150 \times 60$ using Wannier function interpolation as implemented in the EPW software. With the information about the electron density, the effective mass and the high-frequency dielectric constant, which was taken from literature, the real and imaginary part of the Fan-Migdal electron-plasmon self-energy in the vicinity of the CBM was calculated and analysed. It exhibited a characteristic peak at the pole of the real part ($\text{Re} \Sigma = 0$) around the energy $\varepsilon_{\mathbf{k}} - \hbar\omega_{\text{pl}}$, which originates from the plasmon peak in the dielectric function. The effect of the electronic smearing of the \mathbf{k} -points in the self-energy calculation and its continuation to the spectral function features was highlighted and concluded with the recognition that it should be as small

as possible while still guaranteeing the overlap of the smeared \mathbf{k} -points to compute the true coupling strength.

The completion of the thesis was the rigorous assessment of the spectral function. The intrinsic measured spectral function taken at the CBM was offset by a Shirley background accounting for secondary electrons and exhibited spectral features until -1 eV below the Fermi energy. The spectral function calculation was performed using the Fan-Migdal approximation of the self-energy and further refined using the cumulant expansion. To reach a more quantitative alignment with the experiment, a Gaussian convolution was applied to account for the energy resolution of the measurements. The level of agreement reached between experiment and theory was quite remarkable, yet the coupling strength of the electron-plasmon interaction was underestimated a bit. It was proposed that surface effects might influence the spectral function since the doping was carried out at the surface of the material. A simplistic model derived for the interface high-frequency dielectric constant revealed that the electron-plasmon coupling strength is intensified at the interface of the material. Even though it then overestimated the electron-plasmon coupling strength a bit, it reinforced the assumption that there could be an interface component to the spectral function.

This direct comparison between the measured and calculated data allows tracking these subtle differences and resolve them by introducing enhanced models. I think both theorists and experimentalists profit from such close collaborations by looking at the problem from new perspectives. In the case of HfS_2 a detailed study of the pristine and doped electronic and vibrational properties was performed and first-principles approaches were used to understand the formation of satellites in the photoemission spectrum of the material. These detailed studies of specific materials are needed to investigate the many-particle phenomena brought forth by doping TMDs and other semiconductors.

A. Appendix

Surface carrier concentration in HfTe_2

Surface carrier concentrations, separately for electrons and for holes, can be evaluated by calculating the Fermi surface area of the electron pockets and hole pockets. In the following, we give an example of HfTe_2 which has two spin-degenerate hole-like bands at Γ and one electron pocket at each M point of the surface Brillouin zone. The hole pockets at Γ can be approximated using circles of radius c and d whereas the elliptical electron pockets at the M points has a semi major axis a and semi minor axis b . All the The effective masses of the hole-like (m_{1h}^* , m_{2h}^*) and electron like (m_{1e}^* , m_{2e}^*) bands can be evaluated by fitting with a parabola.

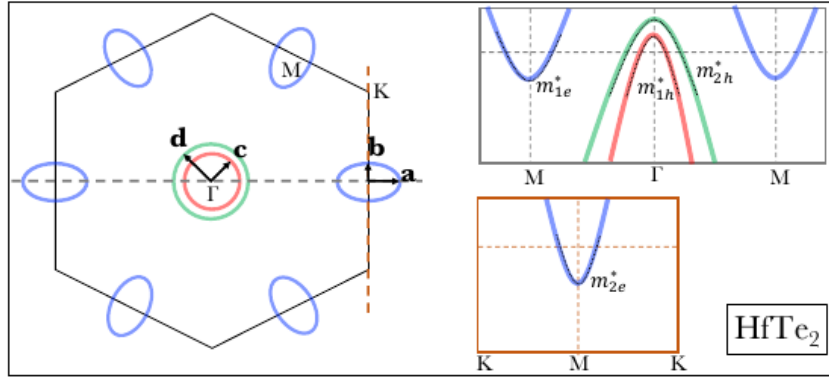


Figure 1: Fermi surface of HfTe_2 featuring 2 hole pockets at Γ and an electron pocket at the M points.

The hole concentration is,

$$n_h = \frac{(c^2 + d^2)}{2\pi} \times 10^{16} \text{cm}^{-2} \quad (1)$$

and the electron concentration is,

$$n_e = \frac{3ab}{2\pi} \times 10^{16} \text{cm}^{-2} \quad (2)$$

where a , b , c , d are in measured in \AA^{-1} from the experimental Fermi surface.

Figure A.1.: Material to calculate the free electron density by Sanjoy. [83]

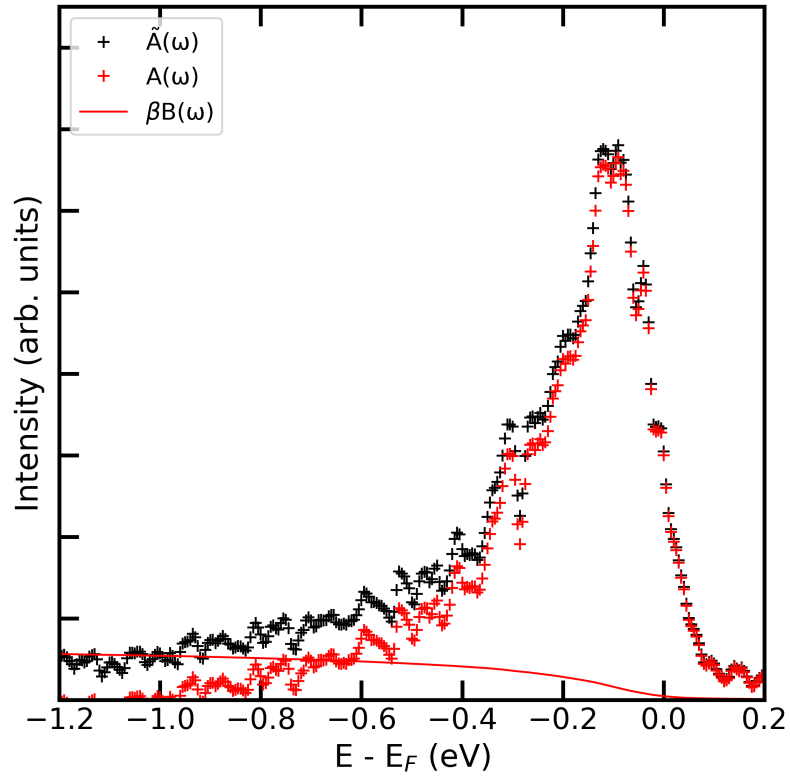


Figure A.2.: Resulting spectral function $A(\omega)$ after subtraction of the Shirley background $B(\omega)$ from the intrinsic spectral function $\tilde{A}(\omega)$.

n ($\text{cm}^{-3} \cdot 10^{19}$)	N_{el}	E_{F} (eV)
0.000	0.000	9.6823
1.475	0.001	9.6946
4.425	0.005	9.7162
14.750	0.010	9.7346
22.121	0.015	9.7494
29.501	0.020	9.7623
36.876	0.025	9.7740
44.251	0.030	9.7848
51.627	0.035	9.7946
59.002	0.040	9.8040
66.377	0.045	9.8125
73.752	0.050	9.8203

Table A.1.: Fermi energies E_{F} corresponding to the free electron density n , with the number of electrons per unit cell volume N_{el} .

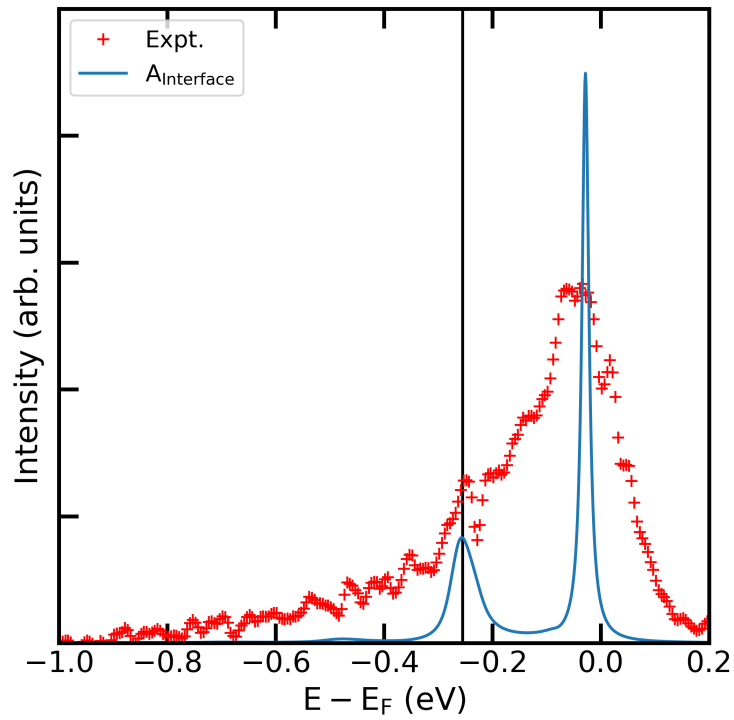


Figure A.3.: Experimental data obtained from ARPES measurements (red crosses) and calculated spectral function within the cumulant expansion (blue line). The vertical black line is introduced at the satellite peak for visual guidance. The high frequency dielectric constant of 3.6 used for the calculation represents the interface of the material. In comparison to Fig. 3.17 a higher multiplication factor is used for the intensity of the calculated spectral function underlining the alignment of the quasi-particle and satellite peak between simulation and experiment.

Bibliography

- [1] D. Pines, Elementary excitations in solids lectures on protons, electrons, and plasmons (CRC Press, 2018).
- [2] A. Damascelli, Z. Hussain, and Z.-X. Shen, “Angle-resolved photoemission studies of the cuprate superconductors”, *Reviews of modern physics* **75**, 473 (2003).
- [3] F. Giustino, “Electron-phonon interactions from first principles”, *Reviews of Modern Physics* **89**, 015003 (2017).
- [4] F. Caruso and F. Giustino, “Theory of electron-plasmon coupling in semiconductors”, *Physical Review B* **94**, 115208 (2016).
- [5] W. H. Sio, “Ab initio theory of polarons”, PhD thesis (University of Oxford, 2019).
- [6] G. D. Mahan, Many-particle physics (Springer Science & Business Media, 2000).
- [7] F. Aryasetiawan, L. Hedin, and K. Karlsson, “Multiple plasmon satellites in na and al spectral functions from ab initio cumulant expansion”, *Physical review letters* **77**, 2268 (1996).
- [8] F. Caruso, C. Verdi, and F. Giustino, “Many-body calculations of plasmon and phonon satellites in angle-resolved photoelectron spectra using the cumulant expansion approach”, *Handbook of Materials Modeling: Methods: Theory and Modeling*, 341–365 (2020).
- [9] F. Caruso, C. Verdi, S. Ponc e, and F. Giustino, “Electron-plasmon and electron-phonon satellites in the angle-resolved photoelectron spectra of n-doped anatase tio 2”, *Physical Review B* **97**, 165113 (2018).
- [10] J. M. Riley, F. Caruso, C. Verdi, L. Duffy, M. D. Watson, L. Bawden, K. Volckaert, G. van der Laan, T. Hesjedal, M. Hoesch, et al., “Crossover from lattice to plasmonic polarons of a spin-polarised electron gas in ferromagnetic euo”, *Nature communications* **9**, 1–8 (2018).
- [11] F. Caruso, P. Amsalem, J. Ma, A. Aljarb, T. Schultz, M. Zacharias, V. Tung, N. Koch, and C. Draxl, “Two-dimensional plasmonic polarons in n-doped monolayer mos 2”, *Physical Review B* **103**, 205152 (2021).
- [12] S. Lal, S. Link, and N. J. Halas, “Nano-optics from sensing to waveguiding”, *Nanoscience And Technology: A Collection of Reviews from Nature Journals*, 213–220 (2010).
- [13] H. A. Atwater and A. Polman, “Plasmonics for improved photovoltaic devices”, *Materials for sustainable energy: a collection of peer-reviewed research and review articles from Nature Publishing Group*, 1–11 (2011).
- [14] M. L. Brongersma, N. J. Halas, and P. Nordlander, “Plasmon-induced hot carrier science and technology”, *Nature nanotechnology* **10**, 25–34 (2015).

- [15] T. Kanazawa, T. Amemiya, A. Ishikawa, V. Upadhyaya, K. Tsuruta, T. Tanaka, and Y. Miyamoto, “Few-layer hfs2 transistors”, *Scientific reports* **6**, 1–9 (2016).
- [16] K. W. Lau, C. Cocchi, and C. Draxl, “Electronic and optical excitations of two-dimensional zrs 2 and hfs 2 and their heterostructure”, *Physical Review Materials* **3**, 074001 (2019).
- [17] C. Habenicht, J. Simon, M. Richter, R. Schuster, M. Knupfer, and B. Büchner, “Potassium-intercalated bulk hfs 2 and hfse 2: phase stability, structure, and electronic structure”, *Physical Review Materials* **4**, 064002 (2020).
- [18] K. Obodo, G. Gebreyesus, C. Ouma, J. Obodo, S. Ezeonu, D. Rai, and B. Bouhafs, “Controlling the electronic and optical properties of hfs 2 mono-layers via lanthanide substitutional doping: a dft+ u study”, *RSC advances* **10**, 15670–15676 (2020).
- [19] W. Kohn and L. J. Sham, “Self-consistent equations including exchange and correlation effects”, *Physical review* **140**, A1133 (1965).
- [20] R. Van Noorden, B. Maher, and R. Nuzzo, “The top 100 papers”, *Nature News* **514**, 550 (2014).
- [21] E. Schrödinger, “An undulatory theory of the mechanics of atoms and molecules”, *Physical review* **28**, 1049 (1926).
- [22] M. Born and W. Heisenberg, “Zur quantentheorie der molekeln”, **389**, 457–494 (1926).
- [23] P. Hohenberg and W. Kohn, “Inhomogeneous electron gas”, *Physical review* **136**, B864 (1964).
- [24] G. Giuliani and G. Vignale, Quantum theory of the electron liquid (Cambridge university press, 2005).
- [25] G. Grosso and G. P. Parravicini, Solid state physics (Academic press, 2013).
- [26] U. Von Barth and L. Hedin, “A local exchange-correlation potential for the spin polarized case. i”, *Journal of Physics C: Solid State Physics* **5**, 1629 (1972).
- [27] Y. Wang and J. P. Perdew, “Correlation hole of the spin-polarized electron gas, with exact small-wave-vector and high-density scaling”, *Physical Review B* **44**, 13298 (1991).
- [28] D. C. Langreth and J. P. Perdew, “Theory of nonuniform electronic systems. i. analysis of the gradient approximation and a generalization that works”, *Physical Review B* **21**, 5469 (1980).
- [29] J. P. Perdew, K. Burke, and M. Ernzerhof, “Generalized gradient approximation made simple”, *Phys. Rev. Lett.* **77**, 3865–3868 (1996).
- [30] R. M. Martin, Electronic structure: basic theory and practical methods (Cambridge university press, 2020).
- [31] N. W. Ashcroft and N. D. Mermin, “Solid state physics, college edn”, Thomson Learning Inc (1976).

-
- [32] N. Troullier and J. L. Martins, “Efficient pseudopotentials for plane-wave calculations”, *Physical review B* **43**, 1993 (1991).
- [33] W. E. Pickett, “Pseudopotential methods in condensed matter applications”, *Computer Physics Reports* **9**, 115–197 (1989).
- [34] E. Fermi, “Sopra lo spostamento per pressione delle righe elevate delle serie spettrali”, *Il Nuovo Cimento* (1924-1942) **11**, 157–166 (1934).
- [35] D. J. Singh and L. Nordstrom, *Planewaves, pseudopotentials, and the lapw method* (Springer Science & Business Media, 2006).
- [36] S. Goedecker and K. Maschke, “Transferability of pseudopotentials”, *Physical Review A* **45**, 88 (1992).
- [37] D. Hamann, M. Schlüter, and C. Chiang, “Norm-conserving pseudopotentials”, *Physical Review Letters* **43**, 1494 (1979).
- [38] P. Nozieres and D. Pines, “Electron interaction in solids. characteristic energy loss spectrum”, *Physical Review* **113**, 1254 (1959).
- [39] F. Caruso and F. Giustino, “The gw plus cumulant method and plasmonic polarons: application to the homogeneous electron gas”, *The European Physical Journal B* **89**, 1–7 (2016).
- [40] J. Lindhard, “On the properties of a gas of charged particles”, *Dan. Vid. Selsk Mat.-Fys. Medd.* **28**, 8 (1954).
- [41] K. Medjanik, O. Fedchenko, S. Chernov, D. Kutnyakhov, M. Ellguth, A. Oelsner, B. Schönhense, T. R. Peixoto, P. Lutz, C.-H. Min, et al., “Direct 3d mapping of the fermi surface and fermi velocity”, *Nature Materials* **16**, 615–621 (2017).
- [42] K. Rossnagel, “Elektronen-spektroskopie mit synchrotronstrahlung”, *Lecture material*, CAU Kiel (2021).
- [43] A. Einstein, “Über einen die erzeugung und verwandlung des lichtet betreffenden heuristischen gesichtspunkt”, (1905).
- [44] M. P. Seah and W. Dench, “Quantitative electron spectroscopy of surfaces: a standard data base for electron inelastic mean free paths in solids”, *Surface and interface analysis* **1**, 2–11 (1979).
- [45] G. Sawatzky, “Testing fermi-liquid models”, *Nature* **342**, 480–481 (1989).
- [46] D. A. Shirley, “High-resolution x-ray photoemission spectrum of the valence bands of gold”, *Physical Review B* **5**, 4709 (1972).
- [47] M. Guzzo, J. J. Kas, F. Sottile, M. G. Silly, F. Sirotti, J. J. Rehr, and L. Reining, “Plasmon satellites in valence-band photoemission spectroscopy”, *The European Physical Journal B* **85**, 1–7 (2012).
- [48] P. C. Martin and J. Schwinger, “Theory of many-particle systems. i”, *Physical Review* **115**, 1342 (1959).
- [49] F. J. Dyson, “The s matrix in quantum electrodynamics”, *Physical Review* **75**, 1736 (1949).

- [50] L. Hedin, “New method for calculating the one-particle green’s function with application to the electron-gas problem”, *Physical Review* **139**, A796 (1965).
- [51] B. Gumhalter, V. Kovač, F. Caruso, H. Lambert, and F. Giustino, “On the combined use of gw approximation and cumulant expansion in the calculations of quasi-particle spectra: the paradigm of si valence bands”, *Physical Review B* **94**, 035103 (2016).
- [52] C. Verdi, F. Caruso, and F. Giustino, “Origin of the crossover from polarons to fermi liquids in transition metal oxides”, *Nature Communications* **8**, 10.1038/ncomms15769 (2017).
- [53] L. Hedin, “Effects of recoil on shake-up spectra in metals”, *Physica Scripta* **21**, 477 (1980).
- [54] F. Aryasetiawan and O. Gunnarsson, “The gw method”, *Reports on Progress in Physics* **61**, 237 (1998).
- [55] J. J. Quinn and R. A. Ferrell, “Electron self-energy approach to correlation in a degenerate electron gas”, *Physical Review* **112**, 812 (1958).
- [56] S. Moser, L. Moreschini, J. Jaćimović, O. Barišić, H. Berger, A. Magrez, Y. Chang, K. Kim, A. Bostwick, E. Rotenberg, et al., “Tunable polaronic conduction in anatase tio 2”, *Physical review letters* **110**, 196403 (2013).
- [57] M. P. De Haas and J. M. Warman, “Photon-induced molecular charge separation studied by nanosecond time-resolved microwave conductivity”, *Chemical Physics* **73**, 35–53 (1982).
- [58] A. Bagnall, W. Liang, E. Marseglia, and B. Welber, “Raman studies of mos2 at high pressure”, *Physica B+ C* **99**, 343–346 (1980).
- [59] E. Marseglia, “Transition metal dichalcogenides and their intercalates”, *International reviews in physical chemistry* **3**, 177–216 (1983).
- [60] Q. H. Wang, K. Kalantar-Zadeh, A. Kis, J. N. Coleman, and M. S. Strano, “Electronics and optoelectronics of two-dimensional transition metal dichalcogenides”, *Nature nanotechnology* **7**, 699–712 (2012).
- [61] J. A. Wilson and A. Yoffe, “The transition metal dichalcogenides discussion and interpretation of the observed optical, electrical and structural properties”, *Advances in Physics* **18**, 193–335 (1969).
- [62] M. Bell and W. Liang, “Electron energy loss studies in solids; the transition metal dichalcogenides”, *Advances in physics* **25**, 53–86 (1976).
- [63] B. Zwartsenberg, R. P. Day, E. Razzoli, M. Michiardi, N. Xu, M. Shi, J. D. Denlinger, G. Cao, S. Calder, K. Ueda, et al., “Spin-orbit-controlled metal–insulator transition in sr2iro4”, *Nature Physics* **16**, 290–294 (2020).
- [64] X. Qian, J. Liu, L. Fu, and J. Li, “Quantum spin hall effect in two-dimensional transition metal dichalcogenides”, *Science* **346**, 1344–1347 (2014).

-
- [65] A. C. Neto, “Charge density wave, superconductivity, and anomalous metallic behavior in 2d transition metal dichalcogenides”, *Physical review letters* **86**, 4382 (2001).
- [66] J. A. Wilson, F. Di Salvo, and S. Mahajan, “Charge-density waves and superlattices in the metallic layered transition metal dichalcogenides”, *Advances in Physics* **24**, 117–201 (1975).
- [67] A. Laturia, M. L. Van de Put, and W. G. Vandenberghe, “Dielectric properties of hexagonal boron nitride and transition metal dichalcogenides: from monolayer to bulk”, *npj 2D Materials and Applications* **2**, 1–7 (2018).
- [68] M. Traving, T. Seydel, L. Kipp, M. Skibowski, F. Starrost, E. E. Krasovskii, A. Perlov, and W. Schattke, “Combined photoemission and inverse photoemission study of hfs₂”, *Phys. Rev. B* **63**, 035107 (2001).
- [69] K. Momma and F. Izumi, “Vesta: a three-dimensional visualization system for electronic and structural analysis”, *Journal of Applied crystallography* **41**, 653–658 (2008).
- [70] P. Giannozzi, S. Baroni, N. Bonini, M. Calandra, R. Car, C. Cavazzoni, D. Ceresoli, G. L. Chiarotti, M. Cococcioni, I. Dabo, et al., “Quantum espresso: a modular and open-source software project for quantum simulations of materials”, *Journal of physics: Condensed matter* **21**, 395502 (2009).
- [71] G. Pizzi, V. Vitale, R. Arita, S. Blügel, F. Freimuth, G. Géranton, M. Gibertini, D. Gresch, C. Johnson, T. Koretsune, et al., “Wannier90 as a community code: new features and applications”, *Journal of Physics: Condensed Matter* **32**, 165902 (2020).
- [72] S. Poncé, E. R. Margine, C. Verdi, and F. Giustino, “Epw: electron–phonon coupling, transport and superconducting properties using maximally localized wannier functions”, *Computer Physics Communications* **209**, 116–133 (2016).
- [73] D. R. Hamann, “Optimized norm-conserving vanderbilt pseudopotentials”, *Phys. Rev. B* **88**, 085117 (2013).
- [74] H. J. Monkhorst and J. D. Pack, “Special points for brillouin-zone integrations”, *Physical review B* **13**, 5188 (1976).
- [75] Q. Zhao, Y. Guo, K. Si, Z. Ren, J. Bai, and X. Xu, “Elastic, electronic, and dielectric properties of bulk and monolayer zrs₂, zrse₂, hfs₂, hfse₂ from van der waals density-functional theory”, *physica status solidi (b)* **254**, 1700033 (2017).
- [76] D. L. Greenaway and R. Nitsche, “Preparation and optical properties of group iv–vi₂ chalcogenides having the cdi₂ structure”, *Journal of Physics and Chemistry of Solids* **26**, 1445–1458 (1965).
- [77] C. Gaiser, T. Zandt, A. Krapf, R. Serverin, C. Janowitz, and R. Manzke, “Band-gap engineering with hfs x se 2- x”, *Physical Review B* **69**, 075205 (2004).
- [78] S. N. Neal, S. Li, T. Birol, and J. L. Musfeldt, “Chemical bonding and born charge in 1t-hfs₂”, (2021).

- [79] M. A. Green, “Intrinsic concentration, effective densities of states, and effective mass in silicon”, *Journal of Applied Physics* **67**, 2944–2954 (1990).
- [80] K. Iordanidou, M. Houssa, G. Pourtois, V. Afanas' ev, and A. Stesmans, “Impact of point defects and oxidation on the electronic properties of hfs2 monolayers”, *ECS Journal of Solid State Science and Technology* **5**, Q3054 (2016).
- [81] N. Glebko, I. Aleksandrova, G. C. Tewari, T. S. Tripathi, M. Karppinen, and A. J. Karttunen, “Electronic and vibrational properties of TiS₂, ZrS₂, and HfS₂: periodic trends studied by dispersion-corrected hybrid density functional methods”, *The Journal of Physical Chemistry C* **122**, 26835–26844 (2018).
- [82] J. Ibáñez, T. Woźniak, F. Dybala, R. Oliva, S. Hernández, and R. Kudrawiec, “High-pressure raman scattering in bulk hfs2: comparison of density functional theory methods in layered ms2 compounds (m= hf, mo) under compression”, *Scientific reports* **8**, 1–10 (2018).
- [83] S. Mahatha, “Surface carrier concentration in hfte2”, See appendix (2021).
- [84] G. Lucovsky, R. White, J. Benda, and J. Revelli, “Infrared-reflectance spectra of layered group-iv and group-vi transition-metal dichalcogenides”, *Physical Review B* **7**, 3859 (1973).
- [85] T. Iwasaki, N. Kuroda, and Y. Nishina, “Anisotropy of lattice dynamical properties in zrs2 and hfs2”, *Journal of the Physical Society of Japan* **51**, 2233–2240 (1982).

List of Figures

2.1.	Flow diagram to solve the Kohn-Sham equation.	7
2.2.	Feynman diagrams of single- and double-fermion closed loops. The wiggly lines represent the Coulomb interaction while the vertex with the arrows are polarization bubbles.[6]	14
2.3.	Loss function of the homogeneous electron gas calculated for a Wigner-Seitz radius of $r_s = 22$ a.u. corresponding to a free electron density of $n = 1.475 \cdot 10^{20} \text{ cm}^{-3}$. The energy (momentum) is given in units of the plasmon energy ω_{pl} (Fermi momentum k_F), respectively.	15
2.4.	Diagrammatic representation of the electron-plasmon scattering process.[4]	16
2.5.	Classical setup of a angle-resolved photoemission spectroscopy experiment including a synchrotron light-source (here an undulator), an assembly of mirror and plane gratings and a hemispherical analyzer.[2]	18
2.6.	Schematic sketch of the photoemission geometry (a). Spectral function of a non-interacting electron system in the vicinity of the Fermi energy E_F (b). Spectral function of a Fermi-liquid (c)left and photoemission spectrum of gasous (solid line) and solid (dashed line) hydrogen H_2 (c)right.[2, 45]	20
2.7.	Figures (a)-(e) show the theoretical (a)-(c) and experimental (d) ARPES spectra obtained for a doping level of $5 \times 10^{18} \text{ cm}^{-3}$ and (f)-(j) are for a free electron density of $3 \times 10^{19} \text{ cm}^{-3}$. (e) and (j) show the <i>ab-initio</i> spectral functions $A(w)$ in the cumulant expansion for these densities evaluated at the Γ high symmetry point due to the excitations of plasmons (pl), phonons (ph) and both of them together (pl-ph). The experimental ARPES spectra 2.7(d) and 2.7(i) were measured by Moser <i>et al.</i> [56]. [9]	24
3.1.	(a) Interlayer A_{1g} and intralayer E_{2g}^2 vibrational modes of the MoS_2 . (b) Crystal structures found in transition-metal dichalcogenides (TMDs) with one layer per unit cell of trigonal symmetry cell (1T) and two layers per unit cell of hexagonal symmetry (2H). The filled and hollow spheres represent transition metal and chalcogenide atoms, respectively. [59]	26
3.2.	(a) Top and (b) side view of the crystal structure of HfS_2 visualised with the VESTA (Visualization for Electronic and STructural Analysis) software package [69]. The blue colored atoms resemble hafnium and the yellow colored ones sulfur. (c) hexagonal BZ [cite: commonwiki].	27
3.3.	Total energy of HfS_2 as a function of the cut-off energy (a) and the number of k-points (b). The energy axis of the plot (b) is offset by 612.71 Ry due to the minimal change in the total energy.	29

3.4.	(a) first-principles electronic band structure of HfS ₂ . (b) Comparison with angle-resolved photoemission spectroscopy ARPES measurements. The red dashed line in the plot (a) marks the Fermi energy of the doped compound.	30
3.5.	(a) Energy difference between the high-symmetry points L and M of the lowest conduction band as a function of the interlayer distance of HfS ₂ . (b) Energy of the indirect band gap as a function of the interlayer distance of HfS ₂	31
3.6.	Effect of spin-orbit coupling (SOC) on the electronic band structure of HfS ₂ . The black (red dashed) line represent the band structure with (without) SOC beginning accounted for in the calculation.	32
3.7.	Conduction band minimum of HfS ₂ along the different high symmetry paths of the first Brillouin zone.	33
3.8.	Iso-energy cut of the k _x -k _y -plane -1.3 eV (a) and -2.2 eV (b) below the Fermi energy. The blue hexagons in (a) mark the area of the Brillouin zone with the Γ point centered in the middle, the M point in the middle of face sides and the K point at the intersection of the face sides. The calculated k-points are plotted in black.[Edit: try white color for Gamma]	34
3.9.	Electronic band structure of HfS ₂ calculated with Quantum ESPRESSO (black solid lines) and interpolated electronic band structure from WANNIER90 (red dashed lines).	34
3.10.	Phonon dispersion relation of HfS ₂ obtained from density functional perturbation theory.	35
3.11.	Iso-energy measurement of the k _x -k _y -plane near the Fermi energy. The blue hexagons mark the area of the Brillouin zone. The white ellipse in (b) is used to estimate the size of one Fermi pocket.	36
3.12.	Dependence of the Fermi energy (a) and plasmon frequency (b) on the free electron density.	38
3.13.	Real (Re) and imaginary (Im) part of the electron self-energy Σ due to electron-plasmon interaction for HfS ₂ at a doping concentration of $n = 1.5 \cdot 10^{20} \text{ cm}^{-3}$. Gaussian smearing 10 meV	38
3.14.	Spectral function $A(\omega)$ in the Midgal-approximation for the conduction band minimum for an density of $1.5 \cdot 10^{20} \text{ cm}^{-3}$ and a high-frequency constant of 7.6. The intensity of $A(\omega)$ for different electron smearings η is plotted as a function of the energy relative to the Fermi energy.	39
3.15.	ARPES measurements of the doped HfS ₂ sample. (a) Band structure showing the Γ point at $k_y = 0 \text{ \AA}^{-1}$ and the CBM around $ k_y = 1.8 \text{ \AA}^{-1}$. (b) Spectral function of the right CBM taken at the blue line.	40
3.16.	Experimental data obtained from ARPES measurements (red crosses), calculated spectral function within the cumulant expansion (blue line) and convoluted spectral function performed with a Gaussian distribution (yellow line). The standard deviation for the Gaussian convolution is $\sigma = 70 \text{ meV}$. The vertical black line is introduced at the satellite peak for visual guidance. The high frequency dielectric constant of 6.2 used for the calculation represents the bulk.	41

3.17. Experimental data obtained from ARPES measurements (red crosses), calculated spectral function within the cumulant expansion (blue line) and convoluted spectral function performed with a Gaussian distribution (yellow line). The standard deviation for the Gaussian convolution is $\sigma = 70$ meV. The vertical black line is introduced at the satellite peak for visual guidance. The high frequency dielectric constant of 3.6 used for the calculation represents the interface of the material.	43
A.1. Material to calculate the free electron density by Sanjoy. [83]	47
A.2. Resulting spectral function $A(\omega)$ after subtraction of the Shirley back- ground $B(\omega)$ form the intrinsic spectral function $\tilde{A}(\omega)$	48
A.3. Experimental data obtained from ARPES measurements (red crosses) and calculated spectral function within the cumulant expansion (blue line) The vertical black line is introduced at the satellite peak for visual guidance. The high frequency dielectric constant of 3.6 used for the calculation rep- resents the interface of the material. In comparison to Fig. 3.17 a higher multiplication factor is used for the intensity of the calculated spectral function underlining the alignment of the quasi-particle and satellite peak between simulation and experiment.	49

List of Tables

2.1. Energies for the dissociation of molecules in eV.[29]	8
3.1. <i>Ab-initio</i> crystal structure parameters of HfS ₂ . The atomic positions are given in units of the crystal lattice vectors.	29
3.2. Summary of computational parameters employed in the <i>ab-initio</i> calculation of the HfS ₂ band structure.	29
3.3. Effective masses of the electrons at the conduction band minimum along different high symmetry paths of the first Brillouin zone.	33
A.1. Fermi energies E_F corresponding to the free electron density n , with the number of electrons per unit cell volume N_{el}	48

Erklärung

Name: Emeis

Vorname: Christoph

Matrikelnummer: 1110516

Erklärung gemäß Paragraph 9 Abs. 7 der Prüfungsverfahrensordnung der Christian-Albrechts-Universität zu Kiel für Studierende der Bachelor- und Master-Studiengänge.

Hiermit erkläre ich, dass ich die Arbeit selbstständig verfasst und keine anderen als die angegebenen Quellen und Hilfsmittel benutzt habe und die Arbeit in keinem anderen Prüfungsverfahren eingereicht habe.

Datum, Unterschrift